Geometry-driven and dark-matter-sustained Milky Way rotation curves with *Gaia* DR3

William Beordo [1,2]*† Mariateresa Crosta [1] Mario G. Lattanzi [1] Paola Re Fiorentin [1]
and Alessandro Spagna [1]

[1]*INAF - Osservatorio Astrofisico di Torino, Via Osservatorio 20, 10025 Pino Torinese, Italy*
[2]*Department of Physics, University of Turin, Via P. Giuria 1, 10125 Turin, Italy*

ABSTRACT

Thanks to *Gaia* DR2, we proved for the first time that a general relativistic Milky Way rotation curve is statistically indistinguishable from its state-of-the-art dark matter analogue. Those results supported the ansatz that gravitational dragging can explain the observed flatness of the Milky Way rotation curve with a consistent radial matter density profile. To challenge again such a scenario, we select 719 143 young disc stars within $|z| < 1$ kpc and up to $R \simeq 19$ kpc from *Gaia* DR3 providing a much larger sample of high-quality astrometric and spectrophotometric data of unprecedented homogeneity. This sample comprises 241 918 OBA stars, 475 520 RGB giants, and 1705 Cepheides that we use to fit, as with DR2, both a classical velocity profile model, *i.e.* with a dark matter halo, and a general relativistic analogue derived from a dust disc-scale metric. Once more, further corroborating our earlier findings, both models are found to explain, with similar statistical quality, the new observed rotational velocities derived from different combinations of the selected sets of stars belonging to the disc of our Galaxy. The geometrical effect is found to drive the velocity profile from 10 kpc outwards, while being responsible for $\sim$30–37 per cent of this profile already at the Sun distance, similarly to the halo contribution in the classical model. This confirms our previous results on the contribution of Einstein's geometry and pushes to further investigate the role of General Relativity in tracing the Milky Way rotation curve; notably, the origin of this gravitational dragging remains undetermined, necessitating a dedicated in-depth exploration.

Key words: gravitation – catalogues – astrometry – Galaxy: disc – Galaxy: kinematics and dynamics – dark matter.

1 INTRODUCTION

The ESA *Gaia* mission (Perryman et al. 2001; Gaia Collaboration 2016) delivers highly accurate kinematics of individual stellar components of the Milky Way (MW) that has been processed through general relativistic astrometric models (Crosta et al. 2017, and references therein). For consistency, the MW reconstruction, one of *Gaia*'s main goals, should be treated according to the theory underlining the data analysis, *i.e.* General Relativity (GR), the standard theory of gravity. In the context of GR measurement theory, we are not allowed to neglect the small curvature limit in the reconstruction of the Milky Way in the first place (see section 1 of Crosta et al. 2020 for an evaluation of the order of accuracy of the conjectural post-Newtonian galactic terms). To verify the possible impact of a fully GR contribution, we decided to start with a more general ansatz, which could as well encompass, a priori, all of the corrections to Newton. As a matter of fact, the evolution of the MW and its constituents is the product of the action of gravity. Common practice is to consider the Newtonian limit of Einstein's equations, namely the metric term g_{00}, thus solving Poisson's equation in order to derive the velocities tracing the observed rotation curve (RC). Then, galaxy dynamics is usually considered dominated by the Newtonian regime, while general relativistic effects are intended as weak corrections only. However, the small curvature limit in GR does not generally coincide with the Newtonian regime. This reason alone should suffice in pushing the investigation of to what extent Newton's approximation of Einstein's field equations represents galactic dynamics.

The above motivated our first attempt (Crosta et al. 2020) to apply DR2 data (Gaia Collaboration 2018) to trace the flat Galactic RC at large radii ($\geq$5 kpc) from the MW centre. These data fit equivalently well to both a simple relativistic model, suitable to represent the Galactic disc as dust in equilibrium, and a classical one comprising a bulge, two stellar discs and a halo largely made of dark matter (DM). However, while the GR disc explains the RC flatness with baryonic matter, DM is required in the MW classical model (MWC) where Newton's dynamics is assumed. To date, as far as the Galaxy is concerned, DM is based on unproved or *ad hoc* physical assumptions and is added in the Poisson's equation as the dominant ingredient of galactic haloes. On the other hand, the set of Einstein's equations allows a GR velocity profile not constrained by the solution

---

* E-mail: william.beordo@inaf.it
† This work is submitted in partial fulfilment for the Doctorate degree in Physics of the University of Turin, Italy.

of Poisson's equation and, at the same time, a GR density profile that includes conformal factors related to an axisymmetric and stationary metric-disc. The DR2 fits showed very good agreement of the GR approach with the observed velocities and the baryonic density at the Sun, while DM as extra mass from a dark halo is still needed in the MWC model.

Before the results of Crosta et al. (2020) (see also Crosta et al. 2019), few authors (e.g. Cooperstock & Tieu 2007; Balasin & Grumiller 2008) explored the weak relativistic regime of Einstein's equations for the galactic dynamics beyond the g_{00} term (and its corrections) or the assumption of spherical mass distribution. Also, in de Almeida, Piattella & Rodrigues (2016) both the Balasin&Grumiller and Cooperstock&Tieu models (hereafter, BG and CT, respectively) were used to compute an effective Newtonian potential and fit to the rotation curves of some external galaxies. Although those previous works could not benefit from the conspicuous and exquisite 6D data provided by *Gaia* we used, they did not try to consider the conformal factor as an extra parameter for testing a GR density profile. For an MW GR model, since *Gaia* is providing direct kinematics and Newton fails to explain the observed RC, we decided to exploit the parametrized BG solution for the RC in order to compare it with the classical approach.

Inspired by our earlier results more authors have recently reconsidered a GR methodology applied to galactic dynamics (Ludwig 2021; Astesiano et al. 2022; Ruggiero, Ortolan & Speake 2022; Srivastava et al. 2023, and references therein).

Besides, there is more in the Crosta et al. (2020) article, as they compare the velocity contribution due to the halo component of MWC to that due only to what they call *gravitational dragging*, i.e. the quantity proportional to the off-diagonal term of the GR metric. Again, the equivalence of such two velocity components over the Galactocentric distances, probed by the DR2 data selected, pointed to the possibility that a gravitational dragging-like effect can sustain a flat RC, thus confirming the validity of the standard theory of gravity also at the scale of a fairly large spiral like the Galaxy.

That first pioneering indication, although already quite significant, needs more and better data and much improved mathematical models to be definitely cross-confirmed. Therefore, this paper is focused on testing again the above GR scenario with the *Gaia* third data release (DR3; Gaia Collaboration 2022d) made public worldwide on 2022 June 13.

Gaia DR3 provides new and improved details for almost two billion stars in our Galaxy. If the coordinates, parallaxes, and annual proper motions are as in its immediate predecessor, EDR3 (Gaia Collaboration 2021), with accuracies good to ∼ 100 μas (for the brightest stars) for ∼1.5 billion of the objects surveyed, DR3 also includes newly released line-of-sight (LOS) velocities (v_{los}) for 32 million stars (with effective temperatures (T_{eff}) in the range of ∼ 3100 to 14 500 K) down to G_{RVS} ∼ 14 mag, increasing by a factor of 5 the sample that was released at DR2 (Andrae et al. 2023; Creevey et al. 2022; Katz et al. 2023). Also, data from the Radial Velocity Spectrometer (RVS) were parametrized by the *General Stellar Parametrizer–spectroscopy* (*GSP–Spec*) module (Recio-Blanco et al. 2022), delivering high quality main stellar atmospheric parameters and chemo-physical parameters for 5.6 million stars over the entire sky.

Therefore, by applying a refined version of the procedure in Crosta et al. (2020) to the new homogeneous stellar samples extracted from DR3, we can: (i) better identify the sample(s) that is (are) least affected by non-axisymmetric gravitational perturbations; (ii) assess the robustness of the results obtained with different disc populations; (iii) improve on understanding the validity limits of the GR model

adopted; (iv) confirm, or discard, the ansatz of the existence of a geometrical effect linked to the space–time curvature, and, in case, better quantify its extent for different disc tracers.

In Section 2, we summarize the theoretical models chosen for the quantitative comparison to the *Gaia*-derived data. Section 3 reports the criteria followed for the new selections of samples of disc stars, while Section 4 describes how the samples were utilized in our fits to the theoretical profiles of Section 2 and compares their predictions. In Sections 5 to 7, we illustrate, respectively, the new DR3-based rotation curves, the corresponding density profiles, and the comparison of the gravitational dragging velocity component to the analogue provided by the DM-dominated halo. Finally, we further discuss our results and summarize our conclusions in Section 8.

2 THEORETICAL DENSITY AND ROTATIONAL VELOCITY PROFILES FOR THE MW

Both classical, with DM and GR models assume that masses of whatever nature, within a large portion of the Galaxy, interact only gravitationally and reside sufficiently far from the central black hole (Gravity Collaboration et al. 2021a).

As reported in Crosta et al. (2020), stars populating the disc can be retained isolated, as stellar encounters become effective well below the parsec scale, while the Galaxy can be considered globally isolated, but not beyond ∼25 kpc, where flaring effects emerge, indicating the onset of external gravitational perturbations. At this scale, neglecting at first any possible intrinsic streaming motions or tidal forces, the rotation curve is traced by the bulk kinematics of the angular-momentum sustained stellar populations.

The classical model for the MW rotation curve comprises a bulge (b), thin (t), and thick (T) discs (d), and a spherical halo (h) like in Crosta et al. (2020). The bulge component is derived from Plummer's density profile (Pouliasis, Di Matteo & Haywood 2017, Model I):

$$\rho_b(r) = \frac{3b_b^2 M_b}{4\pi(r^2 + b_b^2)^{5/2}}, \qquad (1)$$

where, in cylindrical coordinates, the bulge spherical radius is $r = \sqrt{R^2 + z^2}$, with b_b the Plummer radius and M_b the total bulge mass. As for the thin and thick MW discs, we adopt two stellar discs modelled with the Miyamoto–Nagai potential, that can be also approximated with a double exponential disc (McMillan 2017; Korol, Rossi & Barausse 2019). The most general description (Bovy 2015a; Barros, Lépine & Dias 2016; Pouliasis et al. 2017) has the following form

$$\rho_d(R, z) = \frac{M_d b_d^2}{4\pi} \frac{\left[a_d R^2 + \left(a_d + 3\sqrt{z^2 + b_d^2}\right)\left(a_d + \sqrt{z^2 + b_d^2}\right)^2\right]}{\left[R^2\left(a_d + \sqrt{z^2 + b_d^2}\right)^2\right]^{5/2}\left(z^2 + b_d^2\right)^{3/2}}, \qquad (2)$$

where M_d is the total (thin or thick) disc mass and a_d and b_d are scale–length and scale–height, respectively.

Finally, a standard Navarro–Frenk–White (NFW) model describes the DM component as a spherical halo (Navarro, Frenk & White 1996; Bovy 2015a; McMillan 2017):

$$\rho_h(r) = \frac{\rho_{0,h}}{(r/A_h)(1 + r/A_h)^2}, \qquad (3)$$

where $\rho_{0,h}$ is the DM halo density scale and A_h its scale radius.

Given the above density profiles, the MW total gravitational potential is computed by solving the Poisson's equation $\nabla^2\Phi_{tot} = 4\pi G(\rho_b + \rho_{td} + \rho_{Td} + \rho_h)$; then, the circular velocity follows from solving the differential equation $V_{tot}^{MWC}(R) = \sqrt{R(d\Phi_{tot}/dR)}$.

As for the GR model, this is assumed to stem from a continuous distribution of matter with stress-energy tensor $T^{\alpha\beta} = \rho u^{\alpha} u^{\beta}$ (in geometrized units) corresponding to stars considered as dust grains (Neugebauer & Meinel 1995; Neugebauer, Kleinwaechter & Meinel 1996). With this assumption, in a stationary and axisymmetric space–time, the line element can take the form

$$ds^2 = -(dt - N d\phi)^2 + \left[e^{\nu} \left(dR^2 + dz^2 \right) + R^2 d\phi^2 \right], \quad (4)$$

derived by adapting the canonical form of the axisymmetric and stationary metric of Weyl–Lewis–Papapetrou coordinates (Stephani et al. 2009) to a shear-free and expansion-free dust, where N, ν are functions depending only on the coordinates $\{R, z\}$ (see appendix A of Crosta et al. 2020). The time coordinate t (time-like everywhere) spans the range $[-\infty, +\infty]$ and ϕ is the azimuthal angular coordinate in the interval $[0, 2\pi]$ (de Felice & Clarke 1990). Differently from the metric used for the definition of the Barycentric Celestial Reference System, where the Solar System sources generate gravitomagnetic terms as corrections to the Minkowski space–time (Crosta et al. 2017), at Galactic scale, the global MW dynamics could be dominated by the class of Wey–Lewis–Papapetrou space–times, whereas the Newtonian approximation is valid only locally. This was underlined in Crosta et al. (2020) and also recently suggested under the gravitomagnetism assumption by various authors (Ludwig 2021; Astesiano & Ruggiero 2022; Srivastava et al. 2023). Note that, this kind of solutions, if assimilated to a rigid dust, may belong to the Weyl class of axisymmetric metrics whose solutions in the vacuum are known (Senovilla 1993; Stephani et al. 2009, theorem 21.1).

The line element (4) corresponds to that chosen by Balasin & Grumiller (2008) to trace the velocity profiles of disc galaxies in a weakly relativistic scenario tested by Crosta et al. (2020). In that work, we formulated

the GR spatial stellar velocity relative to ZAMO observers (ZAMOs), namely, locally non-rotating observers that have no angular momentum and move on worldlines orthogonal to the hypersurfaces t = constant. Such a choice seems more appropriate if one aims to evaluate the dragging of the space–time. Indeed, ZAMOs can provide an interpretation of the measurement of a purely general relativistic effect in presence of an off-diagonal term of the metric.

A general, spatially circular, orbit following the background symmetries

can be also parametrized by the linear velocity, say ζ, with respect to the ZAMOs. The spatial relative velocity, in terms of the coordinate angular velocity β, the lapse $M = R/\sqrt{(R^2 - N^2)}$, and the shift factor $M^{\phi} = N/(R^2 - N^2)$ is given by

$$\zeta^{\hat{\phi}} = \frac{\sqrt{g_{\phi\phi}}}{M} (\beta + M^{\phi}). \quad (5)$$

In the case of the BG model, the dust is static, therefore $\beta = 0$ and equation (5) reduces to

$$\zeta^{\hat{\phi}} = \frac{N(R, z)}{R}. \quad (6)$$

Equation (6) shows the relative velocity between the 'dust particle' and ZAMOs and turns out to be proportional to the off-diagonal term of the chosen metric (4), *i.e.* $N \propto g_{0\phi}$ (Crosta et al. 2020). Then, it is related to the relativistic gravitational dragging due to the background geometry. With the dust being static, this relative velocity inherently reflects the angular velocity attributed solely to the gravitational dragging effects within the BG space–time. Given this premise, our assumption is to compare this rotational velocity with the observed rotation curve measured by *Gaia*, i.e. with respect to an observer at rest with the distant quasars. This comparison aligns

seamlessly with the fundamental goal of our analysis: to isolate and quantify the gravitational dragging effect, thereby attributing the observed stellar velocities solely to the dragging of the geometry. Recently, Costa et al. (2023) argued that the dragging rises from two singular bars of infinite negative mass possessing a NUT charge connected by a spinning cosmic string. Such a pathology was already discussed by Balasin & Grumiller (2008) and neglected, as the velocity profile solution was found in the disc region in a different regime. As reported also in Crosta et al. (2020), the function $N(R, z)$ was recovered analytically by BG imposing the separation ansatz in solving the Laplace equation and the reflection symmetry with respect to the Galactic plane $z = 0$. The authors excluded values that could prevent a physical solution, such as the localized exotic energy-momentum tensor attributed to Cooperstock & Tieu (2007), or violate the weak energy condition and the assumption of vanishing pressure (for details, see appendix B of Balasin & Grumiller 2008). The final expression for the function $N(R, z)$ is (equation 25; Balasin & Grumiller 2008):

$$\begin{aligned} N(R, z) = \; & V_0 (R_{\text{out}} - r_{\text{in}}) \\ & + \frac{V_0}{2} \sum_{\pm} \left(\sqrt{(z \pm r_{\text{in}})^2 + R^2} - \sqrt{(z \pm R_{\text{out}})^2 + R^2} \right), \quad (7) \end{aligned}$$

where the three parameters V_0, R_{out}, r_{in} were chosen, respectively, as the flat regime velocity, the extension of the MW disc, and the bulge radius. The velocity profile for the adopted GR model results, in the equatorial plane, after setting $V^{\text{BG}}(R) \equiv \zeta^{\phi}(R)$

$$V^{\text{BG}}(R) = \frac{V_0}{R} \left(R_{\text{out}} - r_{\text{in}} + \sqrt{r_{\text{in}}^2 + R^2} - \sqrt{R_{\text{out}}^2 + R^2} \right). \quad (8)$$

The unknowns V_0, R_{out}, r_{in} are then be determined again by fitting to the *Gaia* DR3 data, therefore identifying the spatial limits where the adopted 4D space–time metric is suitable to describe the MW disc as an axisymmetric stationary rotating dust. Note that, Costa et al. (2023) rightly contend for the absence of a perfect analytical model for the whole Galaxy, an ambitious purpose, indeed, since our Galaxy is a multistructured object, as known to the classical DM models as well, based on the composition of several additive parts that have no boundary correlations a priori. Balasin & Grumiller themselves warned of the inadequacies of their GR model to describe a whole galaxy, and other studies following their 2008 paper. Then the same was pointed out specifically for the Galaxy in Crosta et al. (2020), and again by other studies after that. In our original paper, we emphasized that we adopted the tailored solution of the BG velocity profile specifically constructed in order to be valid only on the equatorial plane of the disc (*i.e.* a portion of the Galaxy) and far from the centre, similar to the Neugebauer thin discs, which are well known in literature.

Costa et al. (2023) substantially evidenced what was already known about the BG model. Their theoretical analysis is restricted to aspects that, if not already considered in the literature, lack the understanding of the scope that inspired our interpretation and comparison (with standard (Λ)CDM model). As a matter of fact, they do not provide any Galactic model, nor do they even attempt to provide possible alternative GR solutions to the Galaxy components, like the disc. Most importantly, they seem to neglect the fact that our approach has been made consistent with all the definitions of the IAU resolutions that consider a different off-diagonal term of the metric (see for example, de Felice et al. 2004, 2006, 2011; Crosta & Vecchiato 2010; Crosta 2011; Crosta et al. 2017, 2019). In fact, it is important to recognize the presence of three distinct congruences of observers within our framework: (i) the local barycentric observer tied to the BCRS metric (based on the linearization of the post-

Newtonian approximation to GR), and RAMOD modelling for *Gaia* (based on the measurement protocol in GR involving splitting formalism), (ii) the co-rotating static observer associated with the BG metric in the stationary axisymmetric spacetime, and (iii) the ZAMO observers, which locally do not rotate with respect to the local geometry. It's known that stationary axisymmetric space–times possess both a preferred threading by a time-like Killing vector field (i.e. the static observers), and a preferred slicing by a family of space-like hypersurfaces orthogonal to the ZAMOs. For the former local time direction is fundamental, for the latter space is fundamental (non-local correlation of local time, namely synchronization of times in different points of space, quoting Jantzen, Carini & Bini 1992). Mathematically, it is expected that the static observer and the locally barycentric observer at infinity coincide. However, we are mindful of the fact that the BCRS is connected to a quasi-inertial rather than inertial system. Therefore, our ansatz could turn into verifying whether asymptotically these observers can indeed coincide. In this context, the ZAMOs are employed as gauges of a potential dragging. This is consistent with the Lie transport of the BCRS coordinates at infinity, a principle upheld by the RAMOD formalism. Consequently, the local barycentric observer aligns at infinity with the congruence of curves that are orthonormal, vorticity-free, and expansion-free (namely, the threading and slicing point of views coincide).

Finally, Costa et al. (2023) seem to completely neglect the meaning of our statistical comparisons with the classical model. Data are independent of the theoretical models that we use for the predictions, and that is exactly why they constitute the testing ground. We stress that, despite its problematic origins repeatedly stated out, Balasin & Grumiller's disc velocity curve, with only 3 parameters, when confronted with the *Gaia* data, turns out statistically equivalent to the DM model we also fit to the same data but requiring at least 10 parameters.

Furthermore, relationship (5) for the ZAMOs is valid regardless the source of dragging, i.e. metric terms are not specified. In term of our results (see Section 7) this would mean that the 'excess of mass' might not come from the halo. It is worth stressing here that Crosta et al. (2020) adopted the further ansatz that geometrical effects other than the halo may account for the flatness of the velocity profile, since the BG disc density profile is in line with the baryonic one predicted by the classical model. In fact, expression (5) of a GR spatial velocity relative to the ZAMOs adds geometrical contributions to the coordinate velocity β. Note that, if we assume a linear approximation and a metric $g_{\alpha\beta} \approx \eta_{\alpha\beta} + h_{\alpha\beta}$, then the geometrical terms in the spatial four velocity turn out necessarily small compared to the coordinate velocity β. This is actually the case discussed by Ciotti (2022) and Lasenby, Hobson & Barker (2023). The latter, in particular, focused on CT model we have discarded and confronted the approach of Ludwig (2021), Astesiano et al. (2022), and Ruggiero et al. (2022) with the theoretical approximations made by Ciotti (2022). Both Ciotti (2022) and Lasenby et al. (2023) seem to give a replica of the common assumptions that invalidate GR, i.e. the GR effects are small, instead of searching for alternative mathematical solutions suitable to treat our 'dragging' ansatz, we tested with *Gaia* DR2. Formula (5) holds because of the theory of measurement in GR, theory that is applied in the reduction of the *Gaia* data through general relativistic models developed precisely for that purpose (Crosta 2019, and references therein).Then, more than the availability of BG-like or CT-like solutions, this is what motivated Crosta et al. (2020) to extend GR to model the kinematics of our Galaxy. We underline that in such models, positions, proper motions, and distances are computed from angle measurements in GR assuming the IAU metric, including also a rel-

ativistic satellite attitude, and subsequently quantified in the BCRS coordinates.

In conclusion, by providing an analytical solution for the rotational velocity profile, the BG model served quite well the scope set forth in Crosta et al. (2020), i.e. that of comparing GR to the classical (DM-based) profiles utilized in the literature. Something never done before, we tested that with a relativistic, baryons-only, density there is no need for halo dark matter in the region of validity of the model. Instead, we found the 'gravitational dragging', i.e. the velocity contribution due to the off-diagonal component of the adopted metric, to match the role of a DM halo in classical models. For the first time, there was quantitative evidence of the differences between the Newtonian and GR approaches to MW dynamics.

3 DATA

To study the RC profile of our Galaxy, we select stars tracing the MW disc from the recently released *Gaia* DR3. Precisely, we start from the sub-sample of ~33 million stars with high-precision astrometry and spectroscopic LOS velocities for which individual six dimensional phase-space coordinates can be computed. We retain only objects with: *(i)* the complete set of astrometric parameters (α, δ, μ_{α^*}, μ_δ, ϖ) and corresponding covariance matrix, *(ii)* the three *Gaia* photometric bands (G, BP, RP) all available, and *(iii)* Renormalized Unit Weight Error (RUWE) <1.4, in order to discard sources with problematic astrometric solutions, astrometric binaries, and other anomalous cases (Lindegren 2018). Finally, *Gaia* duplicated sources are also excluded from the initial sample.

We focus on young stellar populations of O-, B-, and A-type (OBA) stars as well as RGB giants with circular orbits (see below). For these targets, we further require parallaxes good to 20 per cent (i.e. $\varpi/\sigma_\varpi \geq 5$) and derive trigonometric distances as $1/\varpi'$ (in appendix A, Gaia Collaboration 2022c), after correcting for the individual parallax zero-point ($\varpi' = \varpi - ZP$) calculated according to Lindegren et al. (2021). Such restrictions are necessary for a proper 6-dimensional reconstruction of the phase-space location occupied by each individual star as derived by the same observer. In addition, we analyse the distribution of Classical Cepheids (DCEPs), for which we adopt excellent distances as derived in Ripepi et al. (2019, 2023).

Galactocentric cartesian (x, y, z) positions (with $R = \sqrt{x^2 + y^2}$ cylindrical radius) and Galactocentric cylindrical velocities (V_R, V_ϕ, V_z), in a right-handed frame (with V_ϕ positive for most of the disc stars), are computed for each star in our samples. As for the Sun's Galactocentric position and its corresponding cylindrical velocities, we adopt the values $(R, z)_\odot = (8.249, 0.0208)$ kpc (Bennett & Bovy 2019; Gravity Collaboration et al. 2021b), and $(V_R, V_\phi, V_z)_\odot = (-9.5, 250.7, 8.56)$ km s^{-1} (Reid & Brunthaler 2020; Gravity Collaboration et al. 2021b). In the following, we describe the details of how we construct each of these samples.

3.1 The sample of OBA stars

The selection of O-, B-, A-type stars, which are part of the Milky Way young disc population, begins with the Golden Sample of 2746 935 candidate-OBA stars with tangential velocity $v_{tan} \leq 180$ km s^{-1}, available through the `gaiadr3.gold_sample_oba_stars` table, carefully selected to be homogeneous and of the highest quality (Gaia Collaboration 2022a).

Here, we focus on the stars that satisfy the astrometric criteria seen above (2125 522) and have measured LOS velocities based on templates with a T_{eff} (`rv_template_teff`) > than 7000 K (242 586). Also, for LOS velocities with 8500 $\leq$ `rv_template_teff`
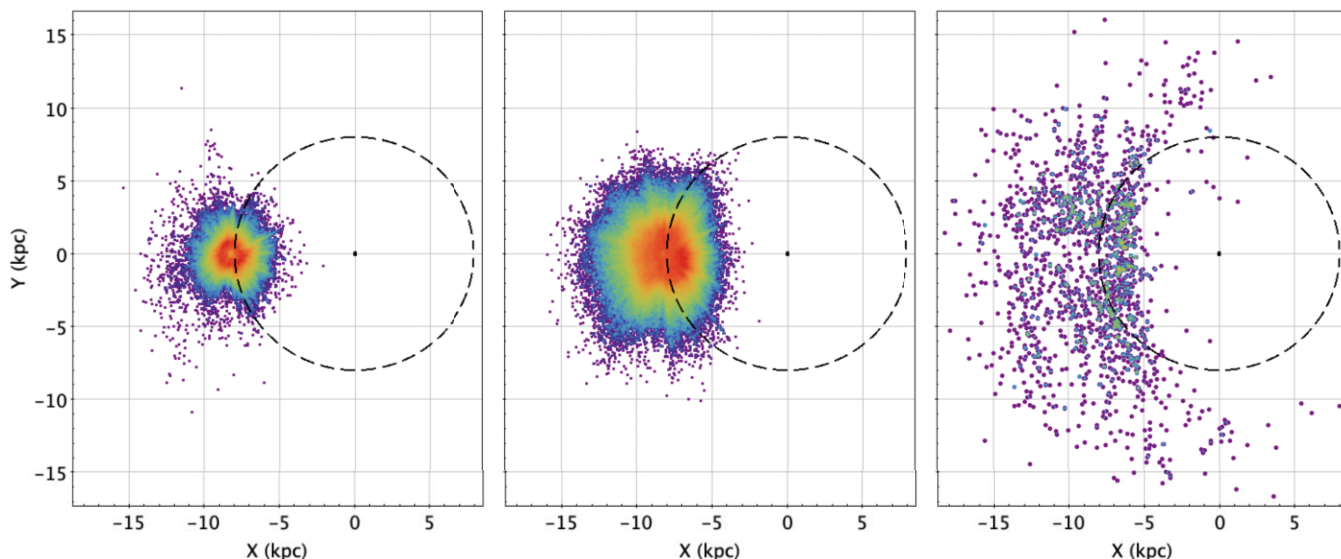
Figure 1. Spatial distribution for the three samples of tracers. OBA stars, RGB giants with (quasi) circular orbits, DCEP are shown from left to right in the Galactic plane. The position of the Galactic Centre is shown by the black dot on the right; the dashed line represents a Galactocentric circle passing through the Sun's position at $(x,y) = (-8.249 \, \text{kpc}, 0 \, \text{kpc})$.

$\leq 14\,500$ K and $6 \leq$ `grvs_mag` ≤ 12, we apply the correction in Blomme et al. (2022), i.e.

$$v_{\text{los}} = radial_v elocity - 7.98 + 1.135 \cdot grvs_m ag. \tag{9}$$

Finally, as we focus on disc stars, we further discard objects with $|z| \geq 1$ kpc and apply a kinematical cut based on the Toomre diagram (Bensby, Feltzing & Lundström 2003; Bensby, Feltzing & Oey 2014; Re Fiorentin, Lattanzi & Spagna 2019; Re Fiorentin et al. 2021; Gaia Collaboration 2022a; Gaia Collaboration 2022c), in order to minimize possible halo contaminants, i.e. only stars whose kinematics satisfies the following inequality are retained

$$\sqrt{V_R^2 + (V_\phi - V_\phi^{\text{LSR}})^2 + V_z^2} < 180 \ \text{km s}^{-1}, \tag{10}$$

where $V_\phi^{\text{LSR}} = 238.5 \, \text{km s}^{-1}$ is the velocity of the Local Standard of Rest at the Sun's position, based on Gravity Collaboration et al. (2021a) and Schönrich, Binney & Dehnen (2010). At the end of our selection process, we are left with a sample of 241 935 bright stars ($G < 14$ mag) near the Galactic plane ($|z| < 1$ kpc), including 198 O-type, 64 356 B-type, and 175 004 A-type as classified by the DR3 catalogue indicator `spectraltype_esphs`. The spatial distribution, projected onto the Galactic plane, is shown in the left panel of Fig. 1. Most of the stars in this OBA sample are within 2–3 kpc from the Sun.

3.2 Red giants with circular orbits: the RGB sample

To select stars on the Red Giant Branch (RGB), we use the effective temperatures and surface gravities derived from *Gaia*'s RVS spectra via the *GSP-Spec* pipeline module (Recio-Blanco et al. 2022), retaining stars from the Medium Quality spectroscopic sample (see Gaia Collaboration 2022c) with $3000 < T_{\text{eff}} < 5500$ K and $\log(g) < 3.0$, as provided in the *Gaia* atmospheric parameters table. Then, after applying the usual filter on distance from the Galactic plane, i.e. $|z| < 1$ kpc, only stars with spectroscopic-derived metallicity [M/H] > -0.5 dex, and with disc-like kinematics, namely $|V_R| < 50 \, \text{km s}^{-1}$, $|V_z| < 30 \, \text{km s}^{-1}$ and $100 < V_\phi < 350 \, \text{km s}^{-1}$, are further considered.

For the resulting sample of 1 548 412 stars, we compute individual orbital parameters (e.g. eccentricity e and z_{max}) by adopting the Galactic potential model `MWPotential2014` from Bovy (2015b). By rejecting objects with $e \geq 0.1$, we end up with a final sample of 475 669 RGB's on (quasi) circular orbits down to $G < 14$ mag. These tracers are typically within 4–5 kpc of the Sun, as shown in the middle panel of Fig. 1.

3.3 Classical Cepheids: the DCEP sample

The selection of DCEPs starts with the sample of 3306 classical Cepheids published in Gaia Collaboration (2022b). For these targets, distances are estimated based on the period-Wesenheit-metallicity (PWZ) relation (Ripepi et al. 2019, 2023).

Of these sources, 2123 have spectroscopic LOS velocities in the main `gaia_source` table, and 679 in the `vari_cepheid` table. For the 636 DCEPs having LOS estimates in both tables, we adopt the values from the spectroscopic *Gaia* pipeline, for which we report a spread of 6 km s^{-1} and a negligible mean offset of 0.3 ± 0.25 km s^{-1}. After removing duplicated sources and retaining only objects with 5-parameter astrometric solutions, RUWE < 1.4, and $|z| < 1$ kpc, the sample consists of 1713 DCEPs down to G $= 16$ mag in the Galactocentric distance range $2 < R < 20$ kpc.; its x– y spatial distribution is shown in the right panel of Fig. 1.

4 THE MILKY WAY ROTATION CURVE FROM THE SELECTED DISC POPULATIONS

The spatial and kinematical selections carried out in the previous section provide us with the 6D phase-space information for an unprecedented sample of 719 317 young objects made of 241 935 OBA stars, 475 669 RGB nearly circular-orbit giants and 1713 Cepheides confined within 1 kpc from the Galactic plane. Therefore, such stars trace, to a fair degree of confidence, the MW disc.

With DR3, Gaia Collaboration (2022b) have found kinematic signatures of the presence of the Galactic bar, whose effect on the stellar rotation velocity appears to be relevant up to ~4–5 kpc from

the Galactic Centre; it is to avoid the bar influence that we put a radial cut at 4.5 kpc. Hence, our final sample is made of: 719 143 stars including 241 918 OBA stars, 475 520 RGB giants, and 1705 Cepheides. In Appendix D, we report the same results but with a radial cut at 5 kpc, to have a direct comparison with Crosta et al. (2020).

Here, we utilize 6 data sets with different mixtures of the stellar disc populations discussed in the previous section: the 3 'pure' data sets of OBA, DCEP, and RGB stars, the combined OBA + DCEP and RGB + DCEP samples, and the total sample consisting of all of the disc stars selected combined (OBA + RGB + DCEP). We bin each data set in cylindrical rings as function of R, using Knuth's Rule for the optimal choice of the bin size. For all data sets but one, the optimal bin size is ~ 0.1 kpc; the DCEP sample requires optimal bins of ~ 0.5 kpc. Note that, whenever necessary, a bin is artificially increased to contain at least three stars. The main properties of the radially binned data sets are reported in Appendix A for OBA, DCEP, RGB stars and their combinations. The tabulated cylindrical coordinates (R's) and the azimuthal velocities (V_ϕ's) of each radial bin are median values, in order to avoid biased values in case of sparsely populated bins.

We adopt the Robust Scatter Estimate (RSE) as a robust measure of the azimuthal velocity dispersion of the population in each bin[1].

The reason we test the different sets is because we aim to identify those combinations that best track the disc kinematics and are less susceptible to non-axisymmetric perturbations. This, indeed, is the case when comparing OBA stars, which are much more localized near the Sun, to RGB and DCEP stars (see Fig. 1). While OBA's are significantly subjected to the gravitational field local to the Solar region, the non-axisymmetric perturbations of the other two populations are averaged over a significantly wider portion of the Galactic plane. In this sense, OBA stars may not be the ideal sample to compare with the rotation curves adopted in this work, as they are generated from purely axisymmetric models of the Galaxy disc.

The average value of the median azimuthal velocities, $V_{\phi,\mathrm{med}}$, across all bins, is ~ 230 km s^{-1} for all data sets. In particular, the median rotation velocity of the bin including the Solar position, $R_\odot = 8.249$ kpc, is $V_{\phi,\mathrm{med},\odot} = 239.94 \pm 0.14$ km s^{-1}, 233.55 ± 1.24 km s^{-1}, and 236.32 ± 0.09 km s^{-1}, respectively for OBA, DCEP, and RGB stars. Such values are consistent with recent determinations of the LRS velocity of $V_\phi^{\mathrm{LSR}} = 238.5 \pm 2.3$ km s^{-1} (Schönrich et al. 2010; Gravity Collaboration et al. 2021a), thus confirming that our samples are good tracers of the Galactic circular velocity. Moreover, the velocity dispersion in each radial bin (as measured by the RSE) is always $\lesssim 42$ km s^{-1}, with a mean value between 9 and 14 km s^{-1} for each data set, as expected for young disc stars. Spatial vertical dispersions, RSE_z, are approximately 118, 275, and 315 pc for OBA, DCEP, and RGB stars, respectively, much less than the spatial filter of $|z| < 1$ kpc imposed at selection. Again, those values are quite compatible with expectations for objects belonging to the MW young disc, and confirm, for the RGB sample, the effectiveness of the procedure discussed in Section 3.2 for extracting giant stars through the eccentricity selection analysis.

Differently from Crosta et al. (2020), we do not perform the bootstrapping technique to infer the median and its uncertainty from the distribution of median azimuthal velocities. This is because most of the times (especially in densely populated bins) the bootstrapped

uncertainty is much lower than the mean individual uncertainty of the azimuthal velocity measurements. To give an example, considering the full sample, the minimum bootstrapped RSE_{V_ϕ} is around 0.07 km s^{-1} (with 100 resamplings) while the minimum value of the mean individual uncertainty $\langle \sigma_{V_\phi} \rangle$ on the velocity measurements is around 1.1 km s^{-1}. The bootstrapped uncertainty can no longer be a proxy for the intrinsic scatter of the population around the median value given the consistent amount of high-precision measurements available with DR3. The actual RSE_{V_ϕ} is always larger than the mean individual uncertainty (except for just two bins in which it is slightly smaller). Therefore, in this work, we consider the RSE_{V_ϕ} as the uncertainty on the median azimuthal velocity when fitting the RC models.

5 FIT TO CLASSICAL AND RELATIVISTIC MW ROTATION CURVES

In this section, we compare the well-studied classical and GR-based models of the MW rotation curves (described in Section 2) to the disc data we extracted from *Gaia* DR3. For each data set, we fit both BG and MWC models to the corresponding DR3 RC (see Appendix A). Bayesian analysis is employed, utilizing a Hamiltonian Monte Carlo method (called NUTS from *No U-Turn Sampler*) implemented in the PYTHON library PYMC4 (Wiecki et al. 2022).

The MWC model has 10 free parameters, i.e. M_b, b_b, M_{td}, a_{td}, b_{td}, M_{Td}, a_{Td}, b_{Td}, $\rho_{0,\mathrm{h}}$, and A_h (note that, we add three more free parameters with respect to Crosta et al. 2020); each contribution to the azimuthal velocity in the classical model is calculated via the GALPY PYTHON package (Bovy 2015a). Instead, the BG model has a total of 4 free parameters, V_0, r_{out}, r_{in} and e^{ν_0} (see Section 6). Details on the choice of priors and of their distributions for the Bayesian fits are given in Section B.

As in Crosta et al. (2020), to explore the parameter space, we adopt the log likelihood function

$$\log \mathcal{L} = -\frac{1}{2} \sum_i \left[\frac{[V_\phi(R_i) - V_\phi^{\mathrm{exp}}(R_i|\boldsymbol{\theta})]^2}{\sigma_{V_\phi}^2} + \log \left(2\pi \sigma_{V_\phi}^2 \right) \right]$$
$$- \frac{1}{2} \left[\frac{[\rho_{\mathrm{bar}}(R_\odot) - \rho^{\mathrm{exp}}(R_\odot|\boldsymbol{\theta})]^2}{\sigma_{\rho_{\mathrm{bar},\odot}}^2} + \log \left(2\pi \sigma_{\rho_{\mathrm{bar},\odot}}^2 \right) \right], \quad (11)$$

where $V_\phi^{\mathrm{exp}}(R_i|\boldsymbol{\theta})$ are the expected velocities computed at each R_i for every trial set of the parameter vector $\boldsymbol{\theta}$ relative to either one of the two theoretical models. In such likelihood function, for the 'observed' (local) baryonic matter density at the Sun and its corresponding error, i.e. $\rho_{\mathrm{bar}}(R_\odot)$ and $\sigma_{\rho_{\mathrm{bar},\odot}}$, we adopted the values, respectively 0.084 and 0.012 M$_\odot$ pc^{-3}, given in McKee, Parravano & Hollenbach (2015). For the BG model, $\rho^{\mathrm{exp}}(R_\odot|\boldsymbol{\theta})(\equiv \rho_\odot^{\mathrm{BG}} \equiv \rho^{\mathrm{BG}}(R_\odot, z = 0))$ is calculated via the 00-term of Einstein's equation (see Section 6), while for the MWC model $\rho^{\mathrm{exp}}(R_\odot|\boldsymbol{\theta}) \equiv \rho_{\odot}^{\mathrm{MWC}} \equiv \rho_{\mathrm{b},\odot}^{\mathrm{MWC}}(R_\odot, z = 0) + \rho_{\mathrm{td}}^{\mathrm{MWC}}(R_\odot, z = 0) + \rho_{\mathrm{Td}}^{\mathrm{MWC}}(R_\odot, z = 0)$ from equations (1) and (2). Contrary to the MWC case, as e^{ν_0} is not present in the $V^{\mathrm{BG}}(R)$ velocity profile, the use of the BG density function ρ^{BG} in the likelihood expression is mandatory.

For the six data sets defined in Section 4, Table 1 lists, as best-fitting estimates, the medians of the posteriors and their 1σ credible intervals, while in Figs C1 and C2, the posterior distributions are shown.

In Fig. 2, the star-like symbols show the median V_ϕ versus R as derived with *Gaia* DR3 data in Appendix A. The two estimated velocity profiles, drawn as the coloured solid lines in Fig. 2, are both good representations of the observed (binned) data. To quantitatively assess this, we compare the two models via the Widely Applicable

---

[1] The definition of RSE is $\mathrm{RSE} = (2\sqrt{2}\, \mathrm{erf}^{-1}(4/5))^{-1} \sim 0.390152 \times (Q90 - Q10)$, with Q90 and Q10 being the 90th and 10th percentiles of a distribution, and it coincides with the standard deviation in the case of a normal distribution.

Table 1. Top: estimates of the free parameters of the MWC model; namely, the medians of the posterior distributions for each data set; the upper and lower bounds (estimated with the 15.87th and 84.13th percentiles) enclose their corresponding 1σ credible intervals. M_b, b_b, M_{td}, a_{td}, b_{td}, M_{Td}, a_{Td}, b_{Td}, $\rho_{0,h}$, and A_h are, respectively, the mass and the scale length of the bulge, the masses and the scale lengths of the two discs, the halo scale density and the halo radial scale. Bottom: estimates of the free parameters of the BG model for each dataset; r_{in}, R_{out}, and V_0 correspond to the lower and upper radial limits, respectively; i.e. the bulge radial size and the Galaxy radius, and the normalization of the velocity in the flat regime, while e^{ν_0} is the estimated dimensionless value characterizing the conformal factor function in the line element (4). Log-values of the WAIC and LOO tests for the Bayesian model comparison are also reported.

MWC model	OBA	DCEP	RGB	OBA + DCEP	RGB + DCEP	ALL
M_b [$10^{10}\,M_\odot$]	$0.9^{+0.6}_{-0.5}$	$1.0^{+0.6}_{-0.6}$	$1.3^{+0.6}_{-0.6}$	$1.0^{+0.6}_{-0.6}$	$1.3^{+0.6}_{-0.6}$	$1.2^{+0.6}_{-0.6}$
b_b [kpc]	$0.9^{+0.9}_{-0.6}$	$0.9^{+0.8}_{-0.6}$	$0.8^{+0.8}_{-0.5}$	$1.0^{+0.9}_{-0.6}$	$0.8^{+0.7}_{-0.5}$	$0.8^{+0.8}_{-0.5}$
M_{td} [$10^{10}\,M_\odot$]	$4.1^{+0.7}_{-0.8}$	$4.1^{+0.8}_{-0.8}$	$3.9^{+0.7}_{-0.7}$	$4.4^{+0.7}_{-0.7}$	$3.9^{+0.7}_{-0.7}$	$4.0^{+0.7}_{-0.7}$
a_{td} [kpc]	$5.0^{+0.9}_{-0.8}$	$5.3^{+0.9}_{-0.9}$	$5.0^{+1.0}_{-0.9}$	$5.2^{+0.8}_{-0.8}$	$5.2^{+1.0}_{-1.0}$	$5.2^{+1.0}_{-1.0}$
b_{td} [kpc]	$0.3^{+0.4}_{-0.1}$	$0.3^{+0.5}_{-0.1}$	$0.4^{+0.6}_{-0.1}$	$0.3^{+0.4}_{-0.1}$	$0.4^{+0.7}_{-0.1}$	$0.4^{+0.6}_{-0.1}$
M_{Td} [$10^{10}\,M_\odot$]	$4.2^{+0.9}_{-0.9}$	$4.2^{+0.9}_{-0.9}$	$4.1^{+0.8}_{-0.8}$	$4.7^{+0.9}_{-0.8}$	$4.0^{+0.8}_{-0.8}$	$4.1^{+0.8}_{-0.8}$
a_{Td} [kpc]	$3.0^{+0.6}_{-0.7}$	$3.0^{+0.7}_{-0.7}$	$2.6^{+0.6}_{-0.6}$	$3.2^{+0.6}_{-0.7}$	$2.6^{+0.6}_{-0.6}$	$2.7^{+0.6}_{-0.6}$
b_{Td} [kpc]	$0.9^{+0.9}_{-0.5}$	$0.8^{+1.0}_{-0.6}$	$0.5^{+0.8}_{-0.3}$	$1.0^{+0.9}_{-0.7}$	$0.5^{+0.8}_{-0.3}$	$0.5^{+0.8}_{-0.3}$
ρ_0^h [$M_\odot\,pc^{-3}$]	$0.010^{+0.005}_{-0.003}$	$0.010^{+0.005}_{-0.004}$	$0.009^{+0.005}_{-0.003}$	$0.013^{+0.005}_{-0.004}$	$0.010^{+0.005}_{-0.003}$	$0.010^{+0.005}_{-0.003}$
A_h [kpc]	17^{+5}_{-4}	16^{+5}_{-3}	17^{+5}_{-4}	14^{+3}_{-2}	16^{+4}_{-3}	16^{+4}_{-3}
WAIC	-341 ± 3	-103 ± 3	-346 ± 2	-448 ± 5	-424 ± 5	-426 ± 5
LOO	-341 ± 3	-103 ± 3	-346 ± 2	-448 ± 5	-424 ± 6	-427 ± 5
BG model	OBA	DCEP	RGB	OBA + DCEP	RGB + DCEP	ALL
r_{in} [kpc]	$0.65^{+0.35}_{-0.27}$	$0.86^{+0.63}_{-0.49}$	$0.18^{+0.20}_{-0.12}$	$0.81^{+0.29}_{-0.28}$	$0.18^{+0.17}_{-0.12}$	$0.20^{+0.18}_{-0.13}$
R_{out} [kpc]	61^{+33}_{-19}	55^{+33}_{-19}	62^{+14}_{-12}	46^{+9}_{-7}	73^{+13}_{-11}	71^{+13}_{-11}
V_0 [km s^{-1}]	273^{+25}_{-17}	281^{+41}_{-24}	257^{+12}_{-7}	288^{+17}_{-16}	255^{+9}_{-6}	256^{+10}_{-7}
e^{ν_0}	$0.094^{+0.017}_{-0.013}$	$0.096^{+0.019}_{-0.014}$	$0.085^{+0.015}_{-0.011}$	$0.094^{+0.017}_{-0.013}$	$0.087^{+0.016}_{-0.011}$	$0.087^{+0.017}_{-0.012}$
WAIC	-343 ± 4	-103 ± 3	-346 ± 2	-448 ± 6	-422 ± 4	-425 ± 4
LOO	-343 ± 4	-103 ± 3	-346 ± 2	-448 ± 5	-423 ± 5	-426 ± 5

Information Criterion (WAIC; Watanabe 2010), which is a fully Bayesian criterion for estimating the out-of-sample expectation. By definition, lower WAIC values indicate a better fit, i.e. the WAIC measures the *poorness* of the fit. For the two models, the results of this test, reported in logarithmic scale for each data set in Table 1, are consistent within errors. Results almost identical to the WAIC are also found with the Leave-One-Out cross-validation (LOO) test. Therefore, given the new DR3 sample at our disposal, we can affirm again what was concluded in Crosta et al. (2020), i.e. our analysis is consistent with the two models being statistically equivalent.

5.1 More on the fits to the Balasin–Grumiller model

As for the BG model, the parameters V_0 and e^{ν_0} found here for the different data sets are all consistent with each other and those obtained from DR2 (Crosta et al. 2020). The same applies, within the errors, to the values of R_{out}, although they tend to be larger than those found in the previous paper; this is actually expected due to the wider radial coverage of DR3 over DR2. On the contrary, different values for r_{in} are obtained. In particular, the presence of RGB stars seems to lead to lower values (of around 0.1–0.2 kpc) compared to those expected from OBA and DCEP stars. This discrepancy is likely the result of the different behaviour of the observed velocity profiles, which at $R \lesssim 5$ kpc are sharply decreasing towards inner radii for OBA and DCEP stars, whereas it is almost constant for RGB stars. According to Balasin & Grumiller (2008, after their equation 26), as r_{in} '*determines the transition between the linear ($R \ll r_{in}$) and the flat ($r_{in} \ll R \ll R_{out}$) regime of the velocity profile*', the size of the bulge '*may be predicted from the velocity profile*'. However, given the potential onset of kinematical effects due to the Galactic bar starting

at $R \sim 4$–5 kpc, improved GR models are required to effectively characterize the non-axisymmetric inner regions of the Galaxy.

From our selection, the stars result spatially constrained to small distances from the plane with $\langle z_{med} \rangle = -0.005 \pm 0.115$ kpc, -0.16 ± 0.26 kpc, and -0.06 ± 0.21 kpc for OBA, DCEP and RGB stars, respectively. These values are always smaller than the resulting r_{in}, ensuring that we remain within the physically viable domain of the BG model, i.e. $|z| < r_{in}$.

5.2 And more on the classical model

As for the MWC model, M_b, M_{td}, a_{td}, M_{Td}, a_{Td}, $\rho_{0,h}$, and A_h are all clearly in agreement, within the errors, with the previous DR2 analysis (Crosta et al. 2020) and the recent estimates by Pouliasis et al. (2017, Model I), Eilers et al. (2019), and McMillan (2017). However, the bulge scale radius b_b is centred at higher values than what was previously estimated at 0.3 kpc (Pouliasis et al. 2017; Crosta et al. 2020, Model I), suggesting the existence of a more extended structure and the inadequacy of the classical bulge model, as in the GR case, given the presence of complex bar. Instead, we find reasonable values for the scale heights of the thin and thick Miyamoto–Nagai discs, consistent with those previously found (0.25 kpc for the thin disc and 0.8 kpc for the thick disc).

6 THE MASS DENSITY

According to the metric function adopted for the BG model, the 00-term of Einstein's field equations is

$$\rho^{BG}(R, z) = \frac{(\partial_R N(R, z))^2 + (\partial_z N(R, z))^2}{8G\pi R^2 e^{\nu(R,z)}}, \quad (12)$$
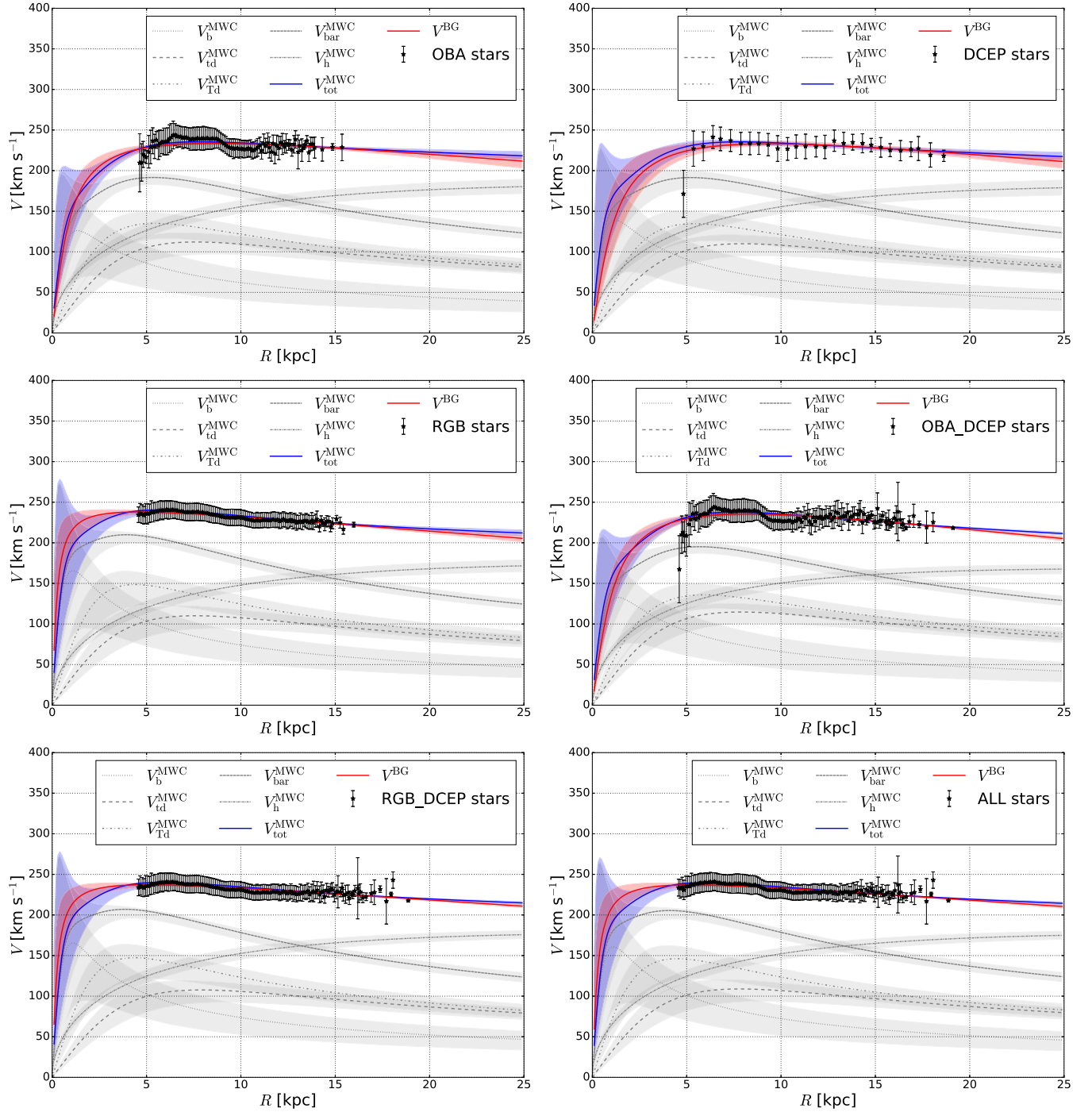
Figure 2. The azimuthal velocity profile of the MW as derived from the sample of disc tracers selected from *Gaia* DR3. For each data set, the black starred symbols represent the median azimuthal velocity at the median distance from the Galactic Centre of the stellar population within each of the radial bins (see Appendix A), where the RSE of the velocity distribution defines the corresponding error bar. The red and blue curves show the best-fitting to the BG and MWC models, respectively. The grey curves, i.e. V_b^{MWC}, V_{td}^{MWC}, V_{Td}^{MWC}, and V_h^{MWC}, represent the contributions to the total MWC rotation curve of the bulge, the thin and thick discs, and the NFW halo of dark matter, respectively. The filled areas represent the 68 per cent reliability intervals of each rotation curve; note that for $R \lesssim 4.5$ kpc both the classical and the relativistic curves are very uncertain because of the lack of data in that region.

where $\rho^{BG}(R, z)$ is the relativistic mass density and $e^{\nu(R, z)}$ is the dimensionless conformal metric factor defined in equation (4). Similarly to what we did in 2020, with DR3, we adopt a procedure different from that of Balasin & Grumiller (2008), when comparing the relativistic mass density (equation 12) to the New-

tonian regime. We assume again a functional behaviour for the conformal factor and use this in the expression of ρ^{exp} utilized in the likelihood function (equation 11). With just one reliable measured density value at our disposal, i.e. that at $R = R_\odot$, the result of our fitting procedure is based on the (crude) assumption
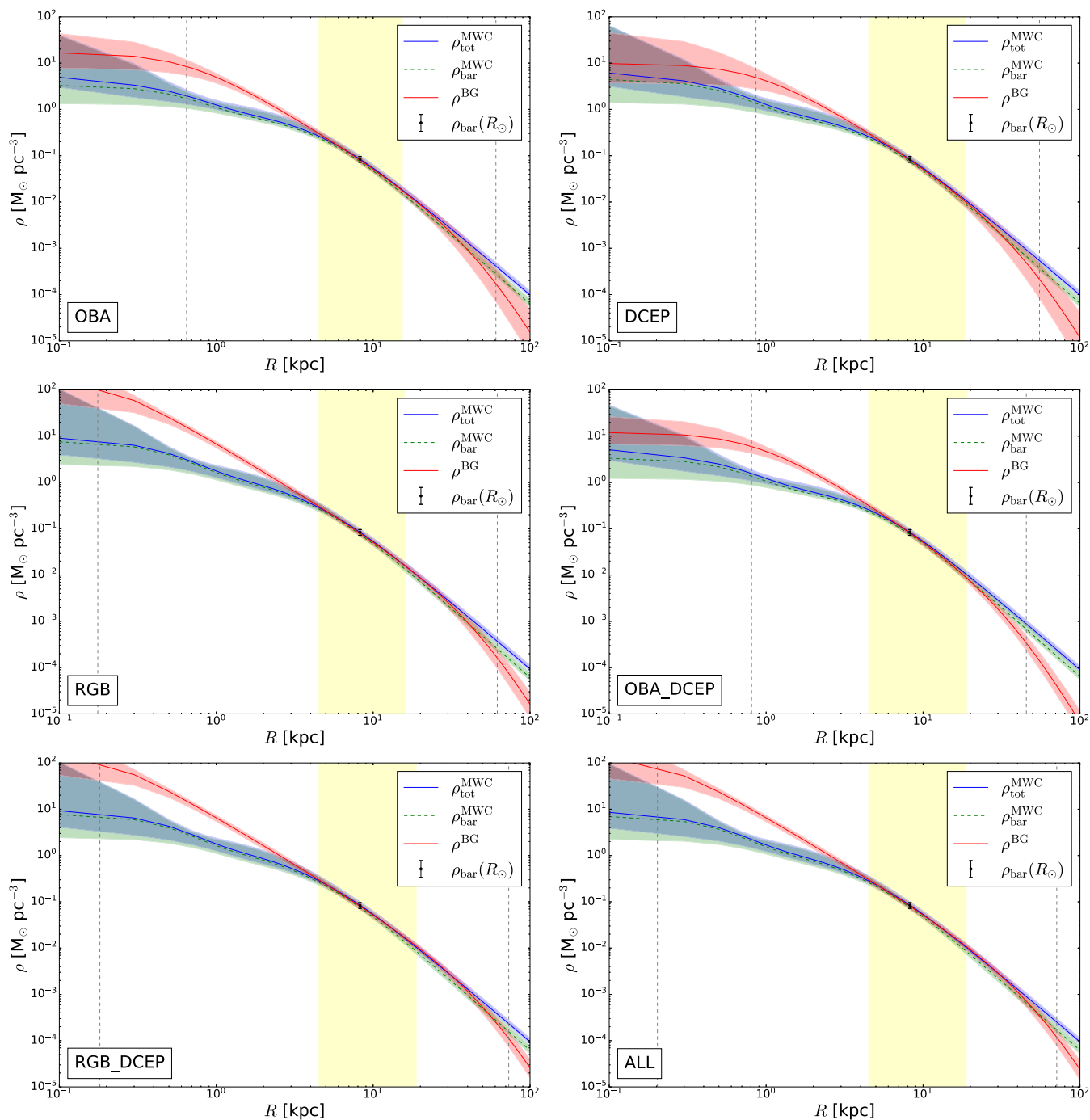
Figure 3. Density profiles of the MW at $z = 0$ for the two models, with their corresponding 68 per cent confidence intervals; in each panel, the red solid line is the BG relativistic mass density ρ^{BG}, while the blue solid line represents the total matter contribution ρ_{tot}^{MWC} for the MWC model (i.e. the sum of the bulge and the two discs as the baryonic counterpart, plus the dark matter halo). The green dashed line shows the contribution ρ_{bar}^{MWC} of the sole baryonic matter for the classical framework. The vertical grey dashed lines represent the values of r_{in} and R_{out}, while the vertical yellow band spans the radial range covered by the sample. Finally, the black dot represents the local mass density inferred at the Sun position, i.e. $\rho_{bar}(R_\odot) = 0.084 \pm 0.012\,M_\odot pc^{-3}$ from McKee et al. (2015).

that the conformal metric factor is constant with R and hence, we have only one dimensionless estimation of $e^{\nu(R,z=0)} \approx e^{\nu_0}$ (see Table 1). The relativistic mass density is obtained by inserting the estimated values of the model parameters (Table 1) in equation (12).

Due to the spatially limited validity of the BG model and the lack of direct mass density estimations at different radii from the Galactic

Centre, we can only compare the mass density profiles of the two models on the MW plane (Fig. 3). In the radial range probed by DR3, the relativistic mass density profile is consistent within 1σ of the total mass density profile and that of the baryonic-only contribution both derived by fitting the classical model. This confirms that the assumption of a constant (with R) value for e^ν holds, at least in this range.

Table 2. Estimates of the local baryonic mass density $\rho_{\mathrm{bar}}(R_\odot)$ for each data set and both models (respectively $\rho_{\mathrm{bar},\odot}^{\mathrm{MWC}}$ and $\rho_\odot^{\mathrm{BG}}$) and of the local dark matter density $\rho_{\mathrm{h},\odot}^{\mathrm{MWC}}$; the upper and lower bounds (estimated with the 15.87th and 84.13th percentiles) enclose their corresponding 1σ credible intervals. $M_{\mathrm{bar}}^{\mathrm{MWC}}$ and M^{BG} are, respectively, the baryonic mass for the MWC model and the relativistic mass for the BG model (through equation 13), both enclosed within the radial region covered by each of our data sets, i.e. $4.6\,\mathrm{kpc} \lesssim R \lesssim 15$–$19\,\mathrm{kpc}$ (the yellow intervals in Fig. 3), and within the corresponding effective vertical width z_{eff} of the relativistic disc, i.e. $|z| \leq z_{\mathrm{eff}}$ (see Section 7 for its definition); while $M_\star^{\mathrm{MWC}}$ and $M_{\mathrm{vir}}^{\mathrm{MWC}}$ are respectively the total stellar mass and the virial mass (i.e. the total mass at the virial radius $R_{\mathrm{vir}}^{\mathrm{MWC}}$) of the Milky Way for the classical model.

Quantity	OBA	DCEP	RGB	OBA + DCEP	RGB + DCEP	ALL
$\rho_{\mathrm{bar},\odot}^{\mathrm{MWC}}$ [$\mathrm{M}_\odot\,\mathrm{pc}^{-3}$]	$0.080_{-0.012}^{+0.012}$	$0.080_{-0.012}^{+0.012}$	$0.080_{-0.012}^{+0.012}$	$0.080_{-0.012}^{+0.012}$	$0.080_{-0.012}^{+0.012}$	$0.080_{-0.012}^{+0.012}$
$\rho_{\mathrm{h},\odot}^{\mathrm{MWC}}$ [$\mathrm{M}_\odot\,\mathrm{pc}^{-3}$]	$0.0092_{-0.0009}^{+0.0009}$	$0.0092_{-0.0009}^{+0.0009}$	$0.0084_{-0.0007}^{+0.0007}$	$0.0083_{-0.0007}^{+0.0007}$	$0.0088_{-0.0007}^{+0.0006}$	$0.0088_{-0.0007}^{+0.0006}$
$\rho_\odot^{\mathrm{BG}}$ [$\mathrm{M}_\odot\,\mathrm{pc}^{-3}$]	$0.080_{-0.012}^{+0.012}$	$0.080_{-0.012}^{+0.013}$	$0.080_{-0.012}^{+0.013}$	$0.081_{-0.012}^{+0.012}$	$0.080_{-0.012}^{+0.012}$	$0.080_{-0.012}^{+0.012}$
$M_{\mathrm{bar}}^{\mathrm{MWC}}$ [$10^{10}\,\mathrm{M}_\odot$]	~ 1.62	~ 1.83	~ 1.25	~ 1.96	~ 1.36	~ 1.48
M^{BG} [$10^{10}\,\mathrm{M}_\odot$]	~ 1.81	~ 2.39	~ 1.11	~ 2.37	~ 1.39	~ 1.54
$M_\star^{\mathrm{MWC}}$ [$10^{10}\,\mathrm{M}_\odot$]	$9.24_{-1.01}^{+1.07}$	$9.30_{-1.10}^{+1.12}$	$9.35_{-0.93}^{+0.95}$	$10.15_{-0.95}^{+0.99}$	$9.22_{-0.91}^{+0.94}$	$9.27_{-0.95}^{+0.90}$
$M_{\mathrm{vir}}^{\mathrm{MWC}}$ [$10^{10}\,\mathrm{M}_\odot$]	~ 114	~ 109	~ 103	~ 85	~ 105	~ 103
$R_{\mathrm{vir}}^{\mathrm{MWC}}$ [kpc]	~ 222	~ 218	~ 214	~ 201	~ 216	~ 215

However, differently from Crosta et al. (2020), the BG density profile is slightly above the baryonic mass density profile of the MWC model up to around 30–60 kpc, after which it starts to decrease below it.

For the local baryonic matter density $\rho_{\mathrm{bar}}(R_\odot)$, we obtain the values listed in Table 2. For both models, these values, i.e. $\rho_{\mathrm{bar},\odot}^{\mathrm{MWC}}$ and $\rho_\odot^{\mathrm{BG}}$, are basically the same among all of the six data sets utilized in this study, and are in agreement with independent current estimates, like $0.098_{-0.014}^{+0.006}\,\mathrm{M}_\odot\mathrm{pc}^{-3}$ of Garbari et al. (2012), $0.077 \pm 0.007\,\mathrm{M}_\odot\mathrm{pc}^{-3}$ of Bienaymé et al. (2014), and the most recent determination of $0.084 \pm 0.012\,\mathrm{M}_\odot\mathrm{pc}^{-3}$ by McKee et al. (2015), which is the local mass density used as the observed datum in the likelihood function (equation 11). Then, the goodness of the 'classical' part of our analysis to provide a baryonic mass density profile via kinematics is confirmed.

For the MWC model, in Table 2, we report our estimates of the local dark matter density $\rho_{\mathrm{h},\odot}^{\mathrm{MWC}}$, together with the total baryonic mass $M_\star^{\mathrm{MWC}}$ (bulge, thin, and thick disc) and the virial mass $M_{\mathrm{vir}}^{\mathrm{MWC}}$ of the Milky Way. The latter is defined accordingly to McMillan (2017) as the spherical mass enclosed within the virial radius $R_{\mathrm{vir}}^{\mathrm{MWC}}$ that gives an average density 200 times larger than the critical density $\rho_{\mathrm{crit}} = \dfrac{3H_0^2}{8\pi G}$ (where we assume $H_0 = 67\,\mathrm{km\,s}^{-1}\,\mathrm{Mpc}^{-1}$; Planck Collaboration XVI 2014).

As for the dark matter density at the Sun, we recover the recent values reported in the literature (Eilers et al. 2019; Cautun et al. 2020; Widmark et al. 2021; Wang, Hammer & Yang 2022), being almost ten times smaller than the local baryonic density. Our estimates of the virial mass are in agreement with the value of $(1.30 \pm 0.30) \times 10^{12}\,\mathrm{M}_\odot$ found by McMillan (2017), but they are almost two times the virial mass of $(7.25 \pm 0.25) \times 10^{11}\,\mathrm{M}_\odot$ derived by Eilers et al. (2019). However, it should be noted that Eilers et al. (2019) estimated only the NFW-profile of the dark matter halo, while keeping contributions from the baryonic components fixed to the results of Pouliasis et al. (2017, Model I). Estimates coming from more recent works (Watkins et al. 2019; Cautun et al. 2020; Fritz et al. 2020; Li et al. 2020; Deason et al. 2021), that use different methods and observational constraints (such as distribution functions or Jeans' spherical equation applied to the kinematics of globular clusters or MW satellite galaxies), are in agreement, within the errors, with our findings, although some tension seems to be present with the smaller values, in the range $(5$–$8) \times 10^{11}\,\mathrm{M}_\odot$, reported in Wang et al. (2022).

In addition, McMillan (2017) reported a total stellar mass of $(5.43 \pm 0.57) \times 10^{10}\,\mathrm{M}_\odot$ that is almost two times smaller than our estimates. Nevertheless, our results are closer to the value of $7.8 \times 10^{10}\,\mathrm{M}_\odot$ proposed by Pouliasis et al. (2017, Model I) for the total disc mass of the MW; indeed, this value matches our estimates of the total stellar mass once the mass of the bulge, $\sim 1 \times 10^{10}\,\mathrm{M}_\odot$ (Table 1), is subtracted.

Fig. 3 also shows that for radii smaller than about 4–5 kpc (inside the non-axisymmetric regions of the MW), the relativistic mass density profile in the plane, assumed of baryonic nature, demands more mass than what provided by the classical components, dark halo included, of the MWC model. However, this is largely compensated by the steeper slope of the BG mass density profile far from the Galactic Centre.

Now, given the quality of the data at our disposal, the question arises if the predictions for the actual amount of baryonic mass in the Galactic plane derived from the two models are actually compatible, or not, with each other. To that purpose, as our metric is stationary and axisymmetric, we compute the relativistic mass by applying the Komar integral (Wald 1984), which in our case reduces to

$$M = -2 \int \left(T_0^0 - \frac{1}{2}T \right) \sqrt{-g}\ d^3x, \tag{13}$$

being T the trace of $T_{\alpha\beta}$ and g the determinant of the metric. The integral has been evaluated within the radial region covered by each of our data sets, i.e. $4.6\,\mathrm{kpc} \lesssim R \lesssim 15 - 19\,\mathrm{kpc}$ (the yellow intervals in Fig. 3), and within the corresponding effective vertical half-width z_{eff} of the relativistic disc, i.e. $|z| \leq z_{\mathrm{eff}}$ (see Section 7 for its definition). The integration from equation (13) yields relativistic masses of $\sim (1.1 - 2.4) \times 10^{10}\,\mathrm{M}_\odot$, that compares quite favourably with the values derived from integrating in the same region the baryonic mass density provided by the MWC model (M^{BG} and $M_{\mathrm{bar}}^{\mathrm{MWC}}$ in Table 2, respectively).

7 GRAVITATIONAL DRAGGING AND DARK HALO CONTRIBUTIONS TO THE MILKY WAY ROTATION CURVE

In order to define a method to compare non-Newtonian gravity models with or without some dark matter, de Almeida, Amendola & Niro (2018) converted the observational rotation curve for some external galaxies into a data set of an effective analogue called the 'effective Newtonian' velocity profile V_{eN}. Following our previous

work (Crosta et al. 2020), we use the relativistic density ρ^{BG} (equation 12), for calculating the effective Newtonian circular velocity profile $V_{\mathrm{eN}}^{\mathrm{BG}}$ at any given point along R from the relation of Binney & Tremaine (2008, see equation 16 in section 3.2 of de Almeida et al. 2018).

By subtracting $V_{\mathrm{eN}}^{\mathrm{BG}}$ to the total velocity V^{BG}, we are able to evaluate the amount of rotational velocity at $z = 0$ due to gravitational dragging, $V_{\mathrm{drag}}^{\mathrm{BG}}$, which has no Newtonian counterpart, and then compare it with the DM halo contribution to $V_{\mathrm{tot}}^{\mathrm{MWC}}$.

None the less, in the formula for calculating $V_{\mathrm{eN}}^{\mathrm{BG}}$ the extension of the integration along the z-axis is problematic since the BG model is valid only in a very small region above and below the Galactic plane. As well known, the model exhibits divergence problems near the rotation axis, where the validity region must be restricted to $|z| \leq r_{\mathrm{in}}$. In light of these problems, it becomes difficult to assess the behaviour of the BG model outside the Galactic plane. Therefore, to compute $V_{\mathrm{eN}}^{\mathrm{BG}}$, we adopt the method described in Crosta et al. (2020), and it is briefly summarized below.

In the radial domain of our experimental velocity data (i.e. from 4.5 up to 19 kpc), we minimize the quadratic form $\chi^2 = \Sigma_i (V_{\mathrm{eN}}^{\mathrm{BG}}(R_i; z_k) - V_{\mathrm{bar}}^{\mathrm{MWC}}(R_i))^2$ over z_k, which represents the effective relativistic half-thickness of the MW disc in the BG model; this scale sets the limit of the vertical integration of the relativistic density to compute numerically the effective Newtonian circular velocity $V_{\mathrm{eN}}^{\mathrm{BG}}$ at each value R_i of the radial coordinate. The pure Newtonian analogue is simply $V_{\mathrm{bar}}^{\mathrm{MWC}} = \sqrt{(V_{\mathrm{b}}^{\mathrm{MWC}})^2 + (V_{\mathrm{td}}^{\mathrm{MWC}})^2 + (V_{\mathrm{Td}}^{\mathrm{MWC}})^2}$, where $V_{\mathrm{b}}^{\mathrm{MWC}}$, $V_{\mathrm{td}}^{\mathrm{MWC}}$ and $V_{\mathrm{Td}}^{\mathrm{MWC}}$ are the circular velocities due to the MW bulge, thin and thick discs, respectively (the broken line curves depicted in Fig. 2).

The minimization process yields $z_{\mathrm{eff}} = 0.28, 0.30, 0.18, 0.30, 0.18, 0.20$ kpc, respectively for OBA, DCEP, RGB, OBA+DCEP, RGB + DCEP and all the stars together.

The red solid curve in Fig. 4 illustrates the $V_{\mathrm{eN}}^{\mathrm{BG}}(R; z_{\mathrm{eff}})$ that the minimization finds closest to $V_{\mathrm{bar}}^{\mathrm{MWC}}(R)$, which is represented as a blue solid line in the picture.

After these steps, we are finally able to calculate the amount of rotational velocity across the MW plane due to gravitational dragging: this is simply done by taking the square root of the quadratic difference between $V^{\mathrm{BG}}(R)$ (equation 8) and the effective Newtonian circular velocity, as computed above, for the disc half-thickness z_{eff}, i.e. $V_{\mathrm{drag}}^{\mathrm{BG}}(R; z_{\mathrm{eff}}) = \sqrt{(V^{\mathrm{BG}}(R))^2 - (V_{\mathrm{eN}}^{\mathrm{BG}}(R; z_{\mathrm{eff}}))^2}$. The $V_{\mathrm{drag}}^{\mathrm{BG}}(R; z_{\mathrm{eff}})$ profile is shown in Fig. 4 by the red-dashed line and it is compared to the blue-dashed curve $V_{\mathrm{h}}^{\mathrm{MWC}}$, the contribution of the DM halo to $V_{\mathrm{tot}}^{\mathrm{MWC}}(R)$ (this is the same as the grey solid line in Fig. 2). The gravitational dragging curve nears zero at $R \sim 5$ kpc, where $V_{\mathrm{eN}}^{\mathrm{BG}}(R; z_{\mathrm{eff}}) \sim V^{\mathrm{BG}}(R)$, then grows sharply within 2.5 kpc outwards overlapping the DM curve for most of the range displayed. In particular, at the Sun's position, for the classical framework the total velocity profile is $\sim$35–40 per cent sustained by the dark matter halo, while for the GR model the geometrical effect is responsible for $\sim$30–37 per cent of the BG velocity profile. Moreover, gravitational dragging becomes predominant from 10–15 kpc driving the flatness of the rotation curve, much like the halo contribution in the classical model. This shows quantitatively that gravitational dragging can plausibly compensate for the need of a dark halo to sustain the flat velocity profile at large radii from the Galactic Centre, as long as the values found for z_{eff} are used in the context of the BG model.

For $R < 4.5$ kpc, we cannot constrain the two models with the *Gaia* data since non-axisymmetric contributions to the gravitational field due to the Galactic bar are expected to show up in this region. Here, the Newtonian velocities differ sharply, to the point that $V_{\mathrm{eN}}^{\mathrm{BG}}(R)$

grows to unrealistic rotational velocities, well above the overall profile $V^{\mathrm{BG}}(R)$: this is signaling that the limit of validity for the BG model has been exceeded. Also, notice that this behaviour is much more pronounced in the presence of RGB stars, for which r_{in} is quite small compared to other data sets and $z_{\mathrm{eff}} \sim r_{\mathrm{in}}$.

This could be the breaking point for the direct applicability of the BG model to the Milky Way, as a single disc density model appears unsuited to represent the complex structure of the MW especially towards its central regions. Such a complexity requires to find a more general solution to the Einstein's equations that can hopefully be applied to the multistructured Galaxy and not just on the Galactic plane, relatively far from the centre.

Despite these limitations, the results obtained for an axisymmetric stationary metric coupled with a pressure-less perfect fluid is already rather significant. This work, in fact, largely confirms Crosta et al. (2020) with *Gaia* DR2: in particular, the existence of a gravitational dragging-like effect that can sustain the flat rotation curve of the MW and possibly those of other disc galaxies.

8 CONCLUSIONS

The improved quality of the *Gaia* data releases offers a unique opportunity to study the dynamics of the Milky Way. Besides the classical model with dark matter, which is the current standard approach for MW dynamics in the cosmological context, a general relativistic model for the disc was confirmed as statistically equivalent in reproducing the rotation curve of the Galaxy and its radial distribution of baryonic matter within the region of validity of the model (Crosta et al. 2020).

Besides the quality, the quantity of the DR3 sample of disc stars led us to validate, update, and strengthen, through different homogeneous stellar sets, the promising results that emerged from DR2 data.

With this in mind, we build rotation curves of the MW from $R = 4.5$ to 19 kpc by carefully selecting stellar populations that best trace the Galactic disc, including 241 918 OBA stars, 475 520 RGB giants, and 1705 Cepheides. RGB and DCEP stars are less affected than OBA objects by local non-axisymmetric perturbations. Nevertheless, the parameters resulting from our Bayesian estimation are in good agreement for all of the stellar groups utilized, and of the mixtures thereof, in the regions of physical validity of the models.

First, for the classical DM model, the values obtained for the free parameters (Table 1) and the local mass densities (Table 2) are mostly in line with recent studies (McMillan 2017; Pouliasis et al. 2017; Eilers et al. 2019; Cautun et al. 2020; Widmark et al. 2021; Wang et al. 2022), confirming the adequacy of the adopted analytical gravitational potentials for the various components of the Milky Way, (i.e. a Plummer's spherical bulge, a Miyamoto–Nagai double-disc for the stellar component, and a Navarro–Frenk–White spherical halo for the dark matter). In addition to this, our analysis suggests the existence of a more extended bulge, even if proper non-axisymmetric models are required to constrain significantly the inner regions given the presence of a conspicuous central bar. Some discrepancies with the literature are present in our estimates of virial and total stellar masses of the MW, but these are highly influenced by the procedure and kind of data used by the various authors, that in most cases do not consider homogeneous samples (McMillan 2017; Pouliasis et al. 2017; Eilers et al. 2019; Watkins et al. 2019; Cautun et al. 2020; Fritz et al. 2020; Li et al. 2020; Deason et al. 2021; Wang et al. 2022).

At the same time, we showed that the general relativistic solution of Balasin & Grumiller (2008) for an axisymmetric stationary metric coupled with a pressure-less perfect fluid is consistent with the new
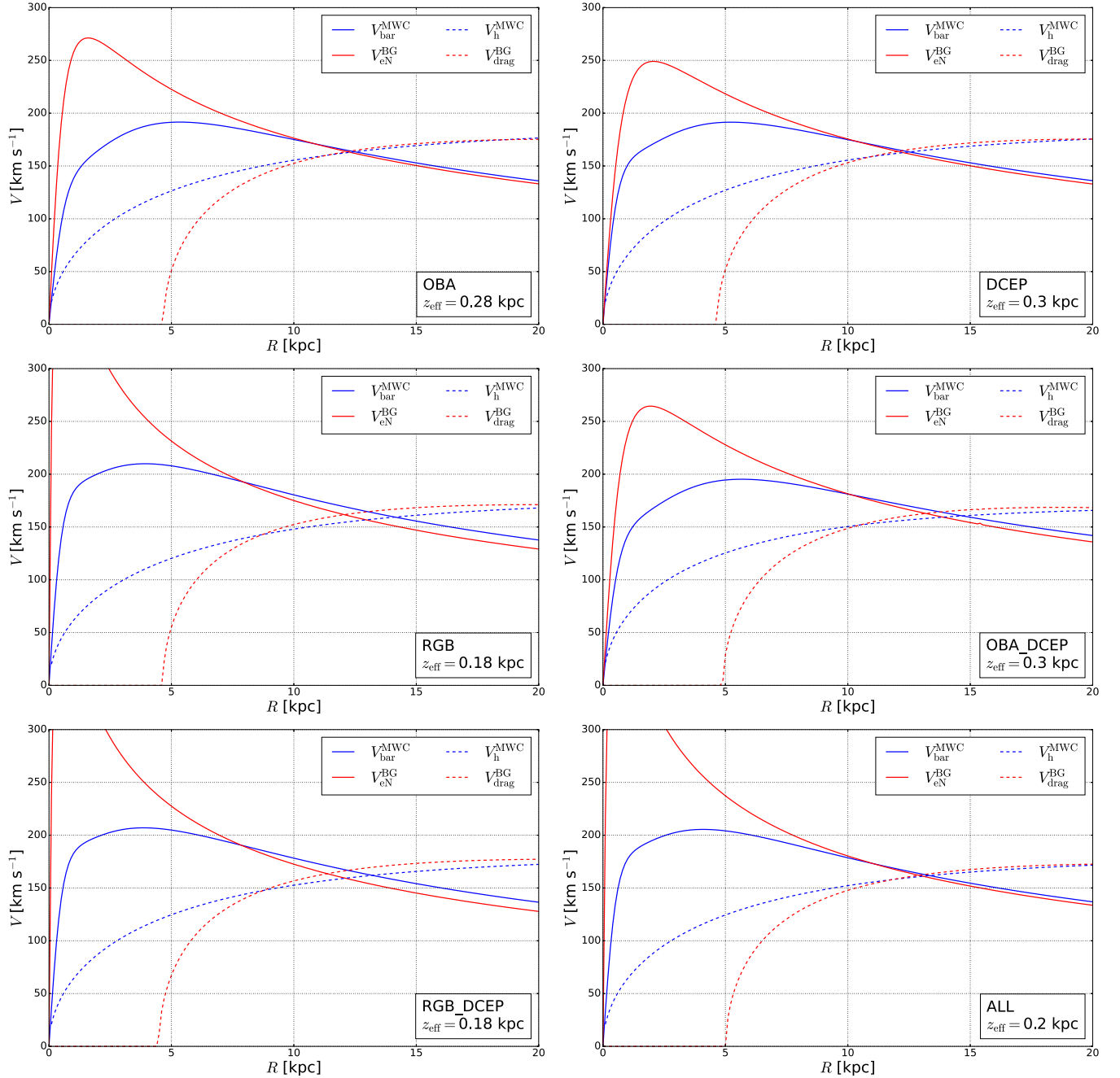
Figure 4. Red and blue lines refer to the BG and MWC models, respectively. Solid lines represent the relativistic effective Newtonian rotation curve, V_{eN}^{BG}, and its analogue V_{bar}^{MWC} for the MWC model, as contributed by the total of baryonic mass. The dashed lines show the MWC halo component alone, i.e. V_h^{MWC}, and the gravitational dragging contribution to V^{BG}, i.e. V_{drag}^{BG}, obtained by subtracting V_{eN}^{BG} from V^{BG} itself (see Section 7 for details).

analysis based on the latest *Gaia* data release, consolidating the findings of Crosta et al. (2020).

Consequently, both models can equivalently explain the observed rotational velocities of different stellar populations of the Milky Way and the local baryonic mass density at the Sun. Moreover, the two models predict comparable estimates of the total baryonic mass, at least around the Galactic plane and within the radial range covered by our samples. Finally, the gravitational dragging, a pure general relativistic effect generated by the off-diagonal terms of the space–time metric, is confirmed to be the candidate that compensates for the dark matter halo contribution to the rotation curve. In the solar

neighbourhood, this geometrical effect is responsible for ∼30–37 per cent of the BG velocity profile, becoming predominant from 10 to 15 kpc outwards. After a second confirmation of our ansatz, in the next papers, we will investigate the origin of the gravitational dragging effect that might derive from an equilibrium condition to more suitable mathematical solutions as already pointed out in section 2.2 of Crosta et al. (2020).

All these findings corroborate once again the fact that the standard theory of gravity, i.e. General Relativity, in its full formulation and understanding, can account for the flatness of the MW rotation curve through a 'DM-like' effect induced by the space–time geometry.

Unlike the Newtonian limit, whereby Poisson's equation is given only by the g_{00} term of the metric, here a complete set of Einstein's equations plays a key role in linking the sources to the space–time geometry and, at the same time, in providing a velocity profile not constrained by the masses, as for the Poisson's equation. Also, one has to bear in mind that in the linear approximation of Einstein's theory and when the energy–momentum conservation reduces to $\partial_\alpha T^{\alpha\beta} = 0$, the matter fields exchange energy and momentum between themselves but not with the gravitational field. Hence, in such a case, dynamics cannot properly include gravity and cannot be applied to systems gravitationally bound like the MW. As a result, the new outcomes presented here for the MW point once more to believe that global Galaxy dynamics could be dominated by hitherto unexplored space–time geometries, e.g. the class of Weyl's solutions in vacuum or Lewis–Papapetrou metric, while the GR corrections to Minkowski's spacetime hold up only to certain scales, e.g. those within our Solar system. In other words, next improvements demand to investigate and test the matching boundary conditions between the possible internal and external solutions of the Einstein's equations, along with their asymptotic behaviour, for our Galaxy and its substructures. To this purpose, our procedure to use an appropriate observational GR framework and homogeneous accurate stellar samples from the *Gaia* archive, as those we selected in this work, will be of utmost importance to constraint theoretical models with real data describing different physical contexts at zero redshift. Working out such solutions will imply to analyse the exchange of energy-momentum between matter and gravitational fields, including the role of the rotational energy, and to what extent it shaped the formation and evolution of our present Galaxy.

DATA AVAILABILITY

We provide our six data sets (see Appendix A) in fully machine-readable form in the supplementary material. Other data underlying this article will be shared on reasonable request to the corresponding author.

REFERENCES

Andrae R. et al., 2023, A&A, 674, A27
Astesiano D., Ruggiero M. L., 2022, Phys. Rev. D, 106, 044061
Astesiano D., Cacciatori S. L., Gorini V., Re F., 2022, Eur. Phys. J. C, 82, 554
Balasin H., Grumiller D., 2008, Int. J. Mod. Phys. D, 17, 475
Barros D. A., Lépine J. R. D., Dias W. S., 2016, A&A, 593, A108
Bennett M., Bovy J., 2019, MNRAS, 482, 1417
Bensby T., Feltzing S., Lundström I., 2003, A&A, 410, 527
Bensby T., Feltzing S., Oey M. S., 2014, A&A, 562, A71
Bienaymé O. et al., 2014, A&A, 571, A92
Bingham E. et al., 2019, J. Mach. Learn. Res., 20, 28:1
Binney J., Tremaine S., 2008, Galactic Dynamics, Princeton Series in Astrophysics, 2ndedn. Princeton Univ. Press, Princeton
Blomme R. et al., 2022, A&A, 674, 12
Bovy J., 2015a, ApJS, 216, 29
Bovy J., 2015b, ApJS, 216, 29
Cautun M. et al., 2020, MNRAS, 494, 4291
Ciotti L., 2022, ApJ, 936, 180
Cooperstock F. I., Tieu S., 2007, Int. J. Mod. Phys. A, 22, 2293
Costa L. F. O., Natário J., Frutos-Alfaro F., Soffel M., 2023, Phys. Rev. D, 108, 044056
Creevey O. L. et al., 2022, A&A, 674, 35
Crosta M., 2011, Class. Quantum Gravity, 28, 235013
Crosta M., 2019, Nuovo Cimento Rivista Serie, 42, 443
Crosta M., Vecchiato A., 2010, A&A, 509, A37
Crosta M., Geralico A., Lattanzi M. G., Vecchiato A., 2017, Phys. Rev. D, 96, 104030
Crosta M., Giammaria M., Lattanzi M. G., Poggio E., 2019, Zenodo, The Gaia Universe, 63
Crosta M., Giammaria M., Lattanzi M. G., Poggio E., 2020, MNRAS, 496, 2107
Deason A. J. et al., 2021, MNRAS, 501, 5964
de Almeida Á. O. F., Piattella O. F., Rodrigues D. C., 2016, MNRAS, 462, 2706
de Almeida Á., Amendola L., Niro V., 2018, J. Cosmol. Astropart. Phys., 2018, 012
de Felice F., Clarke C. J. S., 1990, Relativity on Curved Manifolds. Cambridge Univ. Press, Cambridge
de Felice F., Crosta M. T., Vecchiato A., Lattanzi M. G., Bucciarelli B., 2004, ApJ, 607, 580
de Felice F., Vecchiato A., Crosta M. T., Bucciarelli B., Lattanzi M. G., 2006, ApJ, 653, 1552
de Felice F., Preti G., Crosta M. T., Vecchiato A., 2011, A&A, 528, A23
Eilers A.-C., Hogg D. W., Rix H.-W., Ness M. K., 2019, ApJ, 871, 120
Fritz T. K., Di Cintio A., Battaglia G., Brook C., Taibi S., 2020, MNRAS, 494, 5178
Gaia Collaboration, 2016, A&A, 595, A1
Gaia Collaboration, 2018, A&A, 616, A1
Gaia Collaboration, 2021, A&A, 649, A1
Gaia Collaboration, 2022a, A&A, 674, 34
Gaia Collaboration, 2022b, A&A, 674, 35
Gaia Collaboration, 2022c, A&A, 674, 50
Gaia Collaboration, 2022d, A&A , in press
Garbari S., Liu C., Read J. I., Lake G., 2012, MNRAS, 425, 1445
Gravity Collaboration et al., 2021a, A&A, 654, A22
Gravity Collaboration et al., 2021b, A&A, 654, A22
Jantzen R. T., Carini P., Bini D., 1992, Ann. Phys., 215, 1
Katz D. et al., 2023, A&A, 674, A5
Korol V., Rossi E. M., Barausse E., 2019, MNRAS, 483, 5518
Lasenby A. N., Hobson M. P., Barker W. E. V., 2023, Class. Quantum Gravity, 40, 25
Li Z.-Z., Qian Y.-Z., Han J., Li T. S., Wang W., Jing Y. P., 2020, ApJ, 894, 10
Lindegren L., 2018, Technical note, GAIA-C3-TN-LU-LL-124, http://www.rssd.esa.int/doc_fetch.php?id=3757412, *Re-normalising the astrometric chi-square in Gaia DR2*, Lund Observatory
Lindegren L. et al., 2021, A&A, 649, A4
Ludwig G. O., 2021, Eur. Phys. J. C, 81, 186
McKee C. F., Parravano A., Hollenbach D. J., 2015, ApJ, 814, 13
McMillan P. J., 2017, MNRAS, 465, 76
Navarro J. F., Frenk C. S., White S. D. M., 1996, ApJ, 462, 563
Neugebauer G., Meinel R., 1995, Phys. Rev. Lett., 75, 3046
Neugebauer G., Kleinwaechter A., Meinel R., 1996, Helvetica Physica Acta, 69, 472
Perryman M. A. C. et al., 2001, A&A, 369, 339
Phan D., Pradhan N., Jankowiak M., 2019, eprint (arXiv:1912.11554)

Planck Collaboration XVI, 2014, A&A, 571, A16

Pouliasis E., Di Matteo P., Haywood M., 2017, A&A, 598, A66

Re Fiorentin P., Lattanzi M. G., Spagna A., 2019, MNRAS, 484, L69

Re Fiorentin P., Spagna A., Lattanzi M. G., Cignoni M., 2021, ApJ, 907, L16

Recio-Blanco A. et al., 2022, A&A, 674, 43

Reid M. J., Brunthaler A., 2020, ApJ, 892, 39

Ripepi V. et al., 2019, A&A, 625, A14

Ripepi V. et al., 2023, A&A, 674, A17

Ruggiero M. L., Ortolan A., Speake C. C., 2022, Class. Quantum Gravity, 39, 225015

Schönrich R., Binney J., Dehnen W., 2010, MNRAS, 403, 1829

Senovilla J. M. M., 1993, Rotating Objects Relativ. Phys., 423, 73

Srivastava Y., Immirzi G., Swain J., Panella O., Pacetti S., 2023, European Physical Journal C, 83, 100

Stephani H., Kramer D., MacCallum M., Hoenselaers C., Herlt E., 2009, Exact Solutions of Einstein's Field Equations. Cambridge Univ. Press, Cambridge

Wald R. M., 1984, General Relativity. University of Chicago Press, Chicago

Wang J., Hammer F., Yang Y., 2022, MNRAS, 510, 2242

Watanabe S., 2010, J. Mach. Learn. Res., 11, 3571

Watkins L. L., van der Marel R. P., Sohn S. T., Evans N. W., 2019, ApJ, 873, 118

Widmark A., Laporte C. F. P., de Salas P. F., Monari G., 2021, A&A, 653, A86

Wiecki T. et al., 2022, Zenodo, pymc-devs/pymc: v4.4.0

SUPPORTING INFORMATION

Supplementary data are available at *MNRAS* online.

Please note: Oxford University Press is not responsible for the content or functionality of any supporting materials supplied by the authors. Any queries (other than missing material) should be directed to the corresponding author for the article.

APPENDIX A: DATA SETS

The properties of our six data sets described in Section 4 are presented in Tables A1, A2, A3, A4, A5, A6 (full tables are available online in machine-readable form in the supplementary material).

Table A1. Properties of the binned data for the OBA sample extracted from the *Gaia* DR3 archive. The radial width and the number of stars of each bin are reported in the first two columns; R_{med} is the median value of the cylindrical radial distances in the bin; z_{med} is the median value of the vertical distances from the Galactic plane in the bin, while RSE_z is the corresponding vertical dispersion; $V_{\phi,med}$ is the median value of the azimuthal velocities in the bin; RSE_{V_ϕ} is the Robust Scatter Estimate of the azimuthal velocities; $\langle \sigma_{V_\phi} \rangle$ is the mean value of the individual uncertainties of V_ϕ in the bin.

ΔR [kpc]	N #	R_{med} [kpc]	z_{med} [kpc]	RSE_z [kpc]	$V_{\phi,med}$ [km s^{-1}]	RSE_{V_ϕ} [km s^{-1}]	$\langle \sigma_{V_\phi} \rangle$ [km s^{-1}]
0.10	6	4.64	-0.035	0.083	210	35.8	5.9
0.10	6	4.74	-0.145	0.287	210	23.0	4.7
0.10	8	4.82	-0.081	0.148	220	16.0	3.8
0.10	5	4.88	-0.031	0.184	218	7.8	3.5
0.10	4	4.98	-0.193	0.195	217	7.9	5.7
0.10	17	5.12	-0.059	0.218	223	20.0	3.8
0.10	16	5.22	-0.035	0.135	229	20.7	3.8
0.10	31	5.33	-0.034	0.065	237	15.9	3.1
0.10	55	5.43	-0.034	0.101	230	14.9	2.5
0.10	45	5.52	-0.038	0.049	238	10.3	2.5
$-$	$-$	$-$	$-$	$-$	$-$	$-$	$-$

Full table available online

Table A2. Same as Table A1 but for DCEP stars.

ΔR [kpc]	N #	R_{med} [kpc]	z_{med} [kpc]	RSE_z [kpc]	$V_{\phi,med}$ [km s^{-1}]	RSE_{V_ϕ} [km s^{-1}]	$\langle \sigma_{V_\phi} \rangle$ [km s^{-1}]
0.50	10	4.83	-0.065	0.118	171	29.0	1.8
0.50	12	5.36	0.029	0.095	227	21.7	2.4
0.50	39	5.88	0.012	0.081	230	17.8	1.7
0.50	76	6.39	0.013	0.059	241	14.0	2.0
0.50	113	6.79	0.011	0.055	239	14.5	2.2
0.50	100	7.33	0.011	0.077	237	13.4	2.5
0.50	104	7.87	0.011	0.083	233	13.6	3.0
0.50	126	8.35	0.003	0.103	234	13.9	3.0
0.50	114	8.82	-0.004	0.113	233	13.4	3.0
0.50	85	9.32	-0.018	0.168	232	13.7	3.4
$-$	$-$	$-$	$-$	$-$	$-$	$-$	$-$

Full table available online

Table A3. Same as Table A1 but for RGB stars.

ΔR [kpc]	N #	R_{med} [kpc]	z_{med} [kpc]	RSE_z [kpc]	$V_{\phi,med}$ [km s^{-1}]	RSE_{V_ϕ} [km s^{-1}]	$\langle \sigma_{V_\phi} \rangle$ [km s^{-1}]
0.10	38	4.57	-0.236	0.392	235	9.6	3.7
0.10	59	4.65	-0.206	0.448	237	11.8	3.4
0.10	88	4.76	-0.139	0.519	235	11.5	2.4
0.10	87	4.86	-0.157	0.482	234	10.9	2.7
0.10	122	4.95	-0.175	0.462	236	12.0	2.6
0.10	208	5.06	-0.113	0.423	236	12.5	2.7
0.10	268	5.16	-0.134	0.412	236	11.4	2.8
0.10	296	5.25	-0.108	0.410	239	13.0	2.5
0.10	416	5.36	-0.108	0.427	237	11.7	2.2
0.10	548	5.46	-0.089	0.386	239	11.3	2.0
$-$	$-$	$-$	$-$	$-$	$-$	$-$	$-$

Full table available online

Table A4. Same as Table A1 but for OBA + DCEP stars.

ΔR [kpc]	N #	R_{med} [kpc]	z_{med} [kpc]	RSE_z [kpc]	$V_{\phi,med}$ [km s^{-1}]	RSE_{V_ϕ} [km s^{-1}]	$\langle \sigma_{V_\phi} \rangle$ [km s^{-1}]
0.10	9	4.61	-0.046	0.092	167	41.4	4.8
0.10	6	4.74	-0.145	0.287	210	23.0	4.7
0.10	10	4.80	-0.089	0.166	213	12.8	3.3
0.10	7	4.88	-0.031	0.151	209	20.4	2.9
0.10	7	4.98	-0.085	0.238	209	25.3	3.9
0.10	18	5.12	-0.042	0.218	223	27.3	3.7
0.10	18	5.22	-0.020	0.160	229	19.2	3.9
0.10	35	5.33	-0.026	0.075	236	16.1	3.1
0.10	56	5.43	-0.034	0.097	230	14.8	2.5
0.10	48	5.52	-0.035	0.046	237	10.0	2.4
$-$	$-$	$-$	$-$	$-$	$-$	$-$	$-$

Full table available online

Table A5. Same as Table A1 but for RGB + DCEP stars.

ΔR [kpc]	N #	$R_{\rm med}$ [kpc]	$z_{\rm med}$ [kpc]	RSE_z [kpc]	$V_{\phi,\rm med}$ [km s^{-1}]	RSE_{V_ϕ} [km s^{-1}]	$\langle\sigma_{V_\phi}\rangle$ [km s^{-1}]
0.10	40	4.57	−0.212	0.379	234	10.3	3.6
0.10	60	4.65	−0.193	0.442	236	11.8	3.4
0.10	90	4.76	−0.139	0.513	235	11.7	2.4
0.10	88	4.86	−0.156	0.480	234	11.1	2.7
0.10	125	4.95	−0.170	0.460	236	12.5	2.6
0.10	209	5.05	−0.101	0.422	236	12.5	2.7
0.10	270	5.16	−0.127	0.410	236	11.4	2.8
0.10	298	5.25	−0.107	0.412	239	13.0	2.5
0.10	419	5.36	−0.104	0.425	237	11.7	2.2
0.10	550	5.46	−0.087	0.385	239	11.3	2.0
–	–	–	–	–	–	–	–

Full table available online

Table A6. Same as Table A1 but for all the stars.

ΔR [kpc]	N #	$R_{\rm med}$ [kpc]	$z_{\rm med}$ [kpc]	RSE_z [kpc]	$V_{\phi,\rm med}$ [km s^{-1}]	RSE_{V_ϕ} [km s^{-1}]	$\langle\sigma_{V_\phi}\rangle$ [km s^{-1}]
0.10	42	4.57	−0.174	0.370	234	10.4	3.8
0.10	66	4.65	−0.178	0.411	232	11.7	3.6
0.10	97	4.76	−0.127	0.510	234	12.1	2.5
0.10	98	4.86	−0.137	0.453	231	11.9	2.8
0.10	129	4.96	−0.170	0.463	235	12.8	2.7
0.10	214	5.06	−0.095	0.414	236	12.5	2.7
0.10	288	5.16	−0.098	0.409	235	12.0	2.9
0.10	317	5.25	−0.099	0.406	238	13.3	2.6
0.10	454	5.36	−0.093	0.398	237	11.8	2.2
0.10	610	5.46	−0.076	0.357	239	11.4	2.1
–	–	–	–	–	–	–	–

Full table available online

APPENDIX B: DETAILS ON FREE PARAMETERS AND PRIORS USED IN THE FITS

The actual Bayesian computation makes use of the recent version of the PYTHON package PYMC4 (Wiecki et al. 2022) with the NUTS sampler provided by NUMPYRO (Bingham et al. 2019; Phan, Pradhan & Jankowiak 2019). Given one of the two models, for each dataset of our sample, we run 4 chains of 10 000 iterations each, after a burn-in process of 1000 iterations. The choices of priors are reported below for both models.

(i) For the *BG model*, Crosta et al. (2020) adopted uniform prior distributions as there was no previous knowledge for such parameters, being the first fit ever of a general relativistic model to actual kinematical data for the Milky Way. Therefore, this time priors are centred at the median values estimated from the posterior distributions in Crosta et al. (2020), while uncertainties are taken larger than the corresponding 68 per cent confidence intervals reported in that work to ensure a full exploration of the parameter space within the high-probability regions. In particular, we implemented the following:

(a) $\mathcal{N}(\mu = 263, \sigma = 50)\,\rm km\,s^{-1}$ for V_0;
(b) $\mathcal{N}(\mu = 48, \sigma = 50)\,\rm kpc$ for $R_{\rm out}$;
(c) $\mathcal{N}(\mu = 0.4, \sigma = 2.0)\,\rm kpc$ for $r_{\rm in}$;
(d) $\mathcal{N}(\mu = 0.08, \sigma = 1.00)$ for e^{v_0} [2]

where $\mathcal{N}$ is a normal distribution truncated at positive values.

(ii) For the *MWC model*, priors are taken from the corresponding posterior distributions in Crosta et al. (2020), namely, setting truncated Gaussian distributions centred at their median values and standard deviation given by the 68 per cent confidence interval around the median. While $b_{\rm b}$, $b_{\rm td}$, and $b_{\rm Td}$ were assumed fixed in Crosta et al. (2020), here we prefer to let these three parameters vary and to marginalize them out, since this is a direct application of the law of total probability. For $b_{\rm b}$, $b_{\rm td}$, and $b_{\rm Td}$, we assume Gaussian priors centred at the previously fixed values (reported in Crosta et al. (2020) and suggested by Pouliasis et al. (2017, Model I)) with an arbitrary standard deviation of 1 kpc. In particular, we implemented the following:

(a) $\mathcal{N}(\mu = 1.0, \sigma = 0.8) \times 10^{10}\,\rm M_\odot$ for $M_{\rm b}$;
(b) $\mathcal{N}(\mu = 0.3, \sigma = 1.0)\,\rm kpc$ for $b_{\rm b}$;
(c) $\mathcal{N}(\mu = 3.9, \sigma = 0.8) \times 10^{10}\,\rm M_\odot$ for $M_{\rm td}$;
(d) $\mathcal{N}(\mu = 5.2, \sigma = 1.0)\,\rm kpc$ for $a_{\rm td}$;
(e) $\mathcal{N}(\mu = 0.25, \sigma = 1.0)\,\rm kpc$ for $b_{\rm td}$;
(f) $\mathcal{N}(\mu = 4, \sigma = 1) \times 10^{10}\,\rm M_\odot$ $M_{\rm Td}$;
(g) $\mathcal{N}(\mu = 2.7, \sigma = 0.8)\,\rm kpc$ for $a_{\rm Td}$;
(h) $\mathcal{N}(\mu = 0.8, \sigma = 1.0)\,\rm kpc$ for b_{Tb};
(i) $\mathcal{N}(\mu = 0.009, \sigma = 0.007)\,\rm M_\odot pc^{-3}$ for $\rho_{0,\rm h}$;
(j) $\mathcal{N}(\mu = 17, \sigma = 7)\,\rm kpc$ for $A_{\rm h}$.

APPENDIX C: POSTERIOR DISTRIBUTIONS

The posterior distributions of the Bayesian analysis carried out with the two models are shown in Figs C1 and C2.

---

[2]This is the value characterizing our approximation of a constant metric conformal factor, i.e. $e^{v(R,z)} \approx e^{v_0}$.

Figure C1. Corner plots for the MWC parameters. The histograms on the diagonal show the marginal posterior distributions of each parameter against the corresponding prior distribution drawn in red; the two dashed lines are the 16th and 84th percentiles and the cyan solid line marks the median value (listed in Table 1). The other panels represent the two-dimensional posterior distributions, where the two black contours indicate the 1σ and 2σ credible levels, enclosing respectively the 39.3 per cent and the 63.2 per cent of the samples.
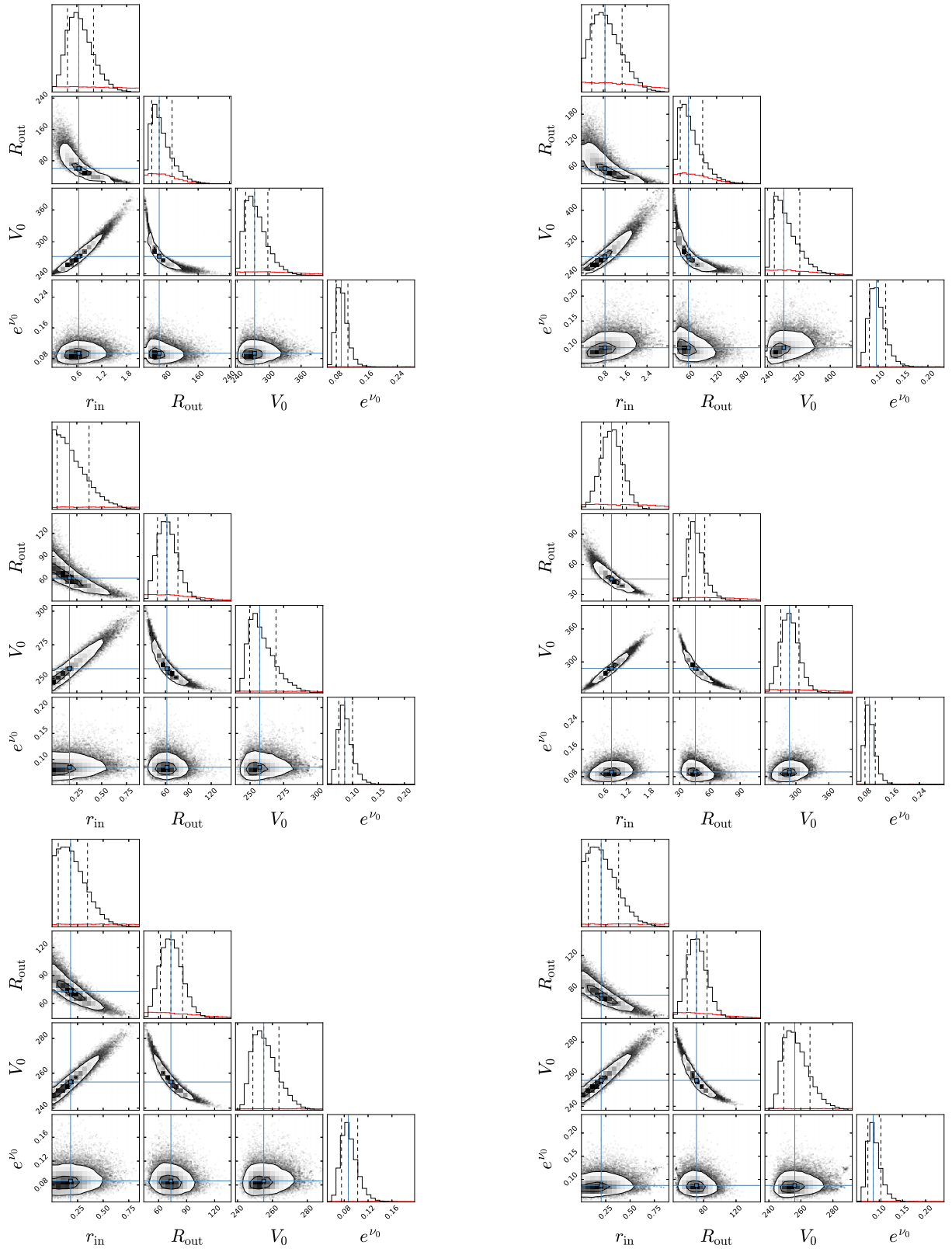
Figure C2. Corner plots for the BG parameters. Same as Fig. C1.

APPENDIX D: RADIAL CUT AT 5 KPC

To have a direct comparison with Crosta et al. (2020), we repeat the analysis by moving the inner radial cut from 4.5 kpc out to 5 kpc. After having prepared data sets similar to those built in Section 4, we estimate again the parameters of the two models with the Bayesian approach described in Section 5.

The results obtained are shown in Table D1, where we report the best-fitting estimates. For both models, the medians of the posteriors are consistent within their 1σ level credible intervals with the values in Table 1 for the case of a radial cut at 4.5 kpc.

The largest deviations are seen for OBA and DCEP stars (and OBA + DCEP), as their rotation velocities drop steeply from 5 kpc inwards. This trend was not present in Crosta et al. (2020) for the sample of upper-main-sequence stars and Cepheids extracted from *Gaia* DR2. For both models, OBA and DCEP stars combined give parameter estimates in agreement, within the uncertainties, with Crosta et al. (2020). Note also that a larger value for R_{out} is expected due to the wider radial coverage of *Gaia* DR3.

On the other hand, the results for RGB stars seem to be little affected by the missing data points between 4.5 and 5 kpc, since their rotation curve is decreasing very slowly inward.

Table D1. Same as Table 1 but for datasets with radial cut at 5 kpc.

MWC model	OBA	DCEP	RGB	OBA + DCEP	RGB + DCEP	ALL
M_b [$10^{10}\,M_\odot$]	$1.2^{+0.6}_{-0.6}$	$1.2^{+0.7}_{-0.6}$	$1.3^{+0.6}_{-0.6}$	$1.2^{+0.6}_{-0.6}$	$1.3^{+0.6}_{-0.6}$	$1.3^{+0.7}_{-0.6}$
b_b [kpc]	$0.8^{+0.8}_{-0.5}$	$0.8^{+0.8}_{-0.6}$	$0.8^{+0.7}_{-0.5}$	$0.8^{+0.8}_{-0.6}$	$0.7^{+0.7}_{-0.5}$	$0.8^{+0.7}_{-0.5}$
M_{td} [$10^{10}\,M_\odot$]	$3.8^{+0.8}_{-0.8}$	$4.2^{+0.8}_{-0.8}$	$3.9^{+0.8}_{-0.7}$	$4.1^{+0.7}_{-0.7}$	$3.9^{+0.7}_{-0.7}$	$3.9^{+0.7}_{-0.7}$
a_{td} [kpc]	$5.1^{+1.0}_{-1.0}$	$5.2^{+0.9}_{-0.9}$	$5.1^{+1.0}_{-1.0}$	$5.2^{+0.9}_{-0.9}$	$5.2^{+1.0}_{-1.0}$	$5.2^{+1.0}_{-1.0}$
b_{td} [kpc]	$0.3^{+0.6}_{-0.1}$	$0.4^{+0.5}_{-0.1}$	$0.4^{+0.6}_{-0.1}$	$0.4^{+0.6}_{-0.1}$	$0.4^{+0.7}_{-0.1}$	$0.4^{+0.7}_{-0.1}$
M_{Td} [$10^{10}\,M_\odot$]	$4.0^{+0.8}_{-0.9}$	$4.3^{+0.9}_{-0.9}$	$4.1^{+0.8}_{-0.8}$	$4.3^{+0.9}_{-0.8}$	$4.1^{+0.8}_{-0.8}$	$4.1^{+0.8}_{-0.8}$
a_{Td} [kpc]	$2.6^{+0.7}_{-0.7}$	$2.9^{+0.7}_{-0.7}$	$2.5^{+0.6}_{-0.6}$	$2.8^{+0.7}_{-0.7}$	$2.6^{+0.7}_{-0.6}$	$2.6^{+0.7}_{-0.6}$
b_{Td} [kpc]	$0.5^{+0.8}_{-0.3}$	$0.7^{+0.9}_{-0.4}$	$0.5^{+0.7}_{-0.2}$	$0.6^{+0.9}_{-0.4}$	$0.4^{+0.8}_{-0.2}$	$0.5^{+0.8}_{-0.3}$
$\rho_{0,h}$ [$M_\odot\,pc^{-3}$]	$0.009^{+0.005}_{-0.003}$	$0.011^{+0.005}_{-0.004}$	$0.009^{+0.005}_{-0.003}$	$0.011^{+0.005}_{-0.004}$	$0.010^{+0.005}_{-0.003}$	$0.010^{+0.005}_{-0.003}$
A_h [kpc]	$18.4^{+5.3}_{-4.0}$	$15.2^{+4.2}_{-2.8}$	$17.5^{+5.0}_{-3.7}$	$15.1^{+3.8}_{-2.6}$	$16.4^{+4.1}_{-2.9}$	$16.3^{+4.1}_{-3.0}$
WAIC	-320 ± 3	-100 ± 2	-328 ± 2	-372 ± 3	-397 ± 3	-399 ± 3
LOO	-320 ± 3	-100 ± 2	-328 ± 2	-372 ± 3	-398 ± 3	-400 ± 3
BG model	OBA	DCEP	RGB	OBA + DCEP	RGB + DCEP	ALL
r_{in} [kpc]	$0.24^{+0.26}_{-0.16}$	$0.71^{+0.69}_{-0.48}$	$0.15^{+0.20}_{-0.11}$	$0.34^{+0.29}_{-0.22}$	$0.15^{+0.18}_{-0.11}$	$0.15^{+0.18}_{-0.11}$
R_{out} [kpc]	$79.05^{+29.29}_{-22.72}$	$48.68^{+18.94}_{-13.23}$	$61.83^{+13.31}_{-11.58}$	$60.33^{+12.89}_{-10.85}$	$70.79^{+11.07}_{-10.56}$	$69.80^{+10.94}_{-10.35}$
V_0 [km s^{-1}]	$255.53^{+14.80}_{-8.25}$	$282.02^{+39.96}_{-23.62}$	$256.61^{+11.33}_{-6.64}$	$264.45^{+15.02}_{-10.70}$	$254.64^{+8.89}_{-5.56}$	$255.09^{+8.92}_{-5.68}$
e^{v_0}	$0.089^{+0.017}_{-0.012}$	$0.094^{+0.018}_{-0.014}$	$0.084^{+0.015}_{-0.011}$	$0.089^{+0.017}_{-0.012}$	$0.086^{+0.015}_{-0.011}$	$0.086^{+0.015}_{-0.012}$
WAIC	-320 ± 3	-99 ± 2	-329 ± 2	-371 ± 3	-396 ± 3	-399 ± 3
LOO	-320 ± 3	-100 ± 2	-329 ± 2	-371 ± 3	-397 ± 3	-399 ± 3

This paper has been typeset from a TeX/LaTeX file prepared by the author.